



HAL
open science

Ductile damage mechanism under shear-dominated loading: In-situ tomography experiments on dual phase steel and localization analysis

Christian Roth, Thilo F. Morgeneyer, Yin Cheng, Lukas Helfen, Dirk Mohr

► To cite this version:

Christian Roth, Thilo F. Morgeneyer, Yin Cheng, Lukas Helfen, Dirk Mohr. Ductile damage mechanism under shear-dominated loading: In-situ tomography experiments on dual phase steel and localization analysis. *International Journal of Plasticity*, 2018, 109, pp.169-192. 10.1016/j.ijplas.2018.06.003 . hal-01869156

HAL Id: hal-01869156

<https://minesparis-psl.hal.science/hal-01869156>

Submitted on 22 Jan 2020

HAL is a multi-disciplinary open access archive for the deposit and dissemination of scientific research documents, whether they are published or not. The documents may come from teaching and research institutions in France or abroad, or from public or private research centers.

L'archive ouverte pluridisciplinaire **HAL**, est destinée au dépôt et à la diffusion de documents scientifiques de niveau recherche, publiés ou non, émanant des établissements d'enseignement et de recherche français ou étrangers, des laboratoires publics ou privés.

Accepted Manuscript

Ductile damage mechanism under shear-dominated loading: In-situ tomography experiments on dual phase steel and localization analysis

Christian C. Roth, Thilo F. Morgeneyer, Yin Cheng, Lukas Helfen, Dirk Mohr



PII: S0749-6419(17)30694-0

DOI: [10.1016/j.ijplas.2018.06.003](https://doi.org/10.1016/j.ijplas.2018.06.003)

Reference: INTPLA 2358

To appear in: *International Journal of Plasticity*

Received Date: 4 December 2017

Revised Date: 7 June 2018

Accepted Date: 7 June 2018

Please cite this article as: Roth, C.C., Morgeneyer, T.F., Cheng, Y., Helfen, L., Mohr, D., Ductile damage mechanism under shear-dominated loading: In-situ tomography experiments on dual phase steel and localization analysis, *International Journal of Plasticity* (2018), doi: 10.1016/j.ijplas.2018.06.003.

This is a PDF file of an unedited manuscript that has been accepted for publication. As a service to our customers we are providing this early version of the manuscript. The manuscript will undergo copyediting, typesetting, and review of the resulting proof before it is published in its final form. Please note that during the production process errors may be discovered which could affect the content, and all legal disclaimers that apply to the journal pertain.

Ductile Damage Mechanism Under Shear-dominated Loading: In-situ Tomography Experiments on Dual Phase Steel and Localization Analysis

Christian C. Roth¹, Thilo F. Morgeneyer²,
Yin Cheng^{2,4}, Lukas Helfen^{3,4} and Dirk Mohr^{1,5}

¹*Department of Mechanical and Process Engineering, ETH Zurich, Switzerland*

²*MINES ParisTech, PSL Research University, Centre des Matériaux, CNRS UMR 7633, Evry, France*

³*Institute for Photon Science and Synchrotron Radiation,
Karlsruhe Institute of Technology (KIT), Germany*

⁴*European Synchrotron Radiation Facility (ESRF), Grenoble, France*

⁵*Impact and Crashworthiness Laboratory, Department of Mechanical Engineering, Massachusetts
Institute of Technology, Cambridge MA, USA*

Abstract. The nucleation, evolution and coalescence of voids is the well-established mechanism leading to ductile fracture under tension-dominated loading conditions. From a theoretical point of view, the same mechanism also applies to shear-dominated loading conditions. Here, an attempt is made to provide for the first time tomographic evidence of damage nucleation and evolution under shear-dominated loading in a modern engineering material. Monotonic experiments are performed on a flat double gage section smiley-shear specimen on the laminography stage of a synchrotron X-ray line. Based on fifteen scans of the entire gage section at a voxel resolution of $1\mu\text{m}^3$, the mesostructural evolution inside a ferrite-bainite steel (FB600) is imaged in 3D up to the instant of specimen fracture. It is found that the as-received material includes a volume fraction of about 0.015% CaO particles. Upon mechanical loading at stress triaxialities evolving from 0 to 0.3, the ductile matrix detaches from these $5\mu\text{m}$ diameter second phase particles, creating a prolate void space whose principal axis is aligned with the principal direction of the applied macroscopic field of deformation. The void space continues to grow while developing micro-crack like features. A large deformation analysis is performed on a representative volume element of the particle-matrix mesostructure replicating the experimental observations of void growth in an approximate manner. Furthermore, the simulation results suggest that a porosity as low as 0.05% is already sufficient to cause the ductile failure under shear-dominated loading through the formation of a band of localized plastic deformation at the mesoscale. The combined experimental-numerical results demonstrate that the well-known ductile damage mechanism of void nucleation, growth and coalescence is also responsible for ductile failure at low stress triaxialities.

Keywords: Ductile damage, simple shear, void evolution, stress state, in situ 3D synchrotron imaging

1. Introduction

Research over the past five decades has established that the nucleation, growth and coalescence of voids are the main events at the mesoscopic level leading to the ductile fracture of polycrystalline materials. Using micromechanics, it has been shown that the rate of void growth is governed by the stress triaxiality and the equivalent plastic strain (e.g. Rice and Tracey, 1969). Current work on ductile fracture leverages substantial recent progress in experimental and computational mechanics. These activities contribute to the understanding of the failure mechanisms (e.g. Baczanski et al. (2016), Kim and Yoon (2015), Matsuno et al. (2015), De Geus et al. (2016), Daehli et al. (2016), Khan and Bhasin (2017), Khadyko et al. (2016), Lee et al. (2015), Scales et al., 2016) and the development of enhanced porous plasticity models to predict ductile failure (Tutyshkin et al. (2015), Zhai et al. (2016), Shutov et al. (2015), Ling et al. (2016)). In real materials, the effect of anisotropy on ductile failure is also often relevant. It may be related to the anisotropy of the matrix material (e.g. Benzerga and Besson, 2001), void shape effects (e.g. Gologanu et al. (1993), Madou and Leblond (2012)) or a combination of both (e.g. Keralavarma and Benzerga, 2008).

Ductile failure is a plastic deformation process which includes a damage phase that terminates with the initiation of cracks due to void coalescence. The coalescence mode depends on the normal and shear stresses acting on a layer of voids, resulting in either internal necking or localized shearing of the intervoid ligaments (e.g. Tvergaard (1990), Benzerga and Leblond (2010), Morin et al. (2016), Torki et al. (2017)). Even though the mechanism transition is smooth, a differentiation between shear-dominated and tension-dominated loading can be meaningful when discussing void coalescence. However, this distinction may not be necessary when discussing microstructural evolution during the damage phase. From the point of view of micromechanics, damage for shear- and tension-dominated loading is characterized by the same mechanism of void nucleation, growth and shape evolution. However, for the sake of simplicity, the effects of shape evolution and rotation have been neglected in the early models of ductile damage (e.g. Gurson (1977)), while advanced porous plasticity models (e.g. Gologanu et al. (1993), Danas and Ponte Castaneda (2014), Morin et al. (2016)) provide a more complete treatise of the underlying micromechanical problem. What is missing to date is clear experimental evidence on the fracture process under

shear-dominant loading conditions along with a demonstration that shear-induced damage is indeed responsible for the crack initiation after simple shear loading.

The fracture of ductile materials including particles received significant attention in the literature, but most studies focused on stress states with positive stress triaxialities only (e.g. Argon (1976), Steglich and Brocks (1997), Ghahremaninezhad and Ravi-Chandar (2012), Daehli et al. (2016)). Fleck et al. (1989) investigated the nucleation of voids from cylindrical particles under simple shear numerically. Their results demonstrate the effective stress reduction associated with particle debonding and void nucleation at zero mean stress. Horstemeyer et al. (2000) reported that the number of voids nucleated per unit area in cast aluminum A356 under torsion is higher than that for tensile loading. Moreover, Horstemeyer et al. (2000) proposed a void nucleation rule that depends not only on the applied strain, but also on the stress triaxiality and the Lode angle parameter¹. This proposal is a significant modification as compared to the widely-used void nucleation rule of Chu and Needleman (1980) which relates the rate of void nucleation to the equivalent plastic strain only. It is noted that Horstemeyer et al. (2000) considered the effect of the Lode angle parameter on the void nucleation rule only, while their void growth rule depended on the stress triaxiality and strain only (McClintock, 1968). In other words, the damage is considered to nucleate due to shear, but its growth is expected to be prohibited. Another modification of the void nucleation rule has been proposed by Morgeneyer and Besson (2011) by incorporating a dependence on the Lode parameter of the strain rate tensor. They captured the flat to slant crack transition numerically during ductile tearing. Mohr and Treitler (2008) analyzed the fracture mechanism in the pressure die casting alloy Al-10Si-Mg-Mn at different stress triaxialities. According to their metallographic observations, final fracture is always due to the linking of micro-cracks. In their material, particle cracking led to void nucleation and subsequent microcrack formation at positive stress triaxialities, while particle debonding appeared to dominate at nearly zero stress triaxiality. It is extremely challenging to interrupt a fracture experiment during the final stage of void coalescence (or micro-crack linking) since the stored elastic strain energy is usually sufficient to drive the coalescence

¹The term “Lode parameter” is not explicitly employed by Horstemeyer et al. (2000), but their idea of introducing the ratio of J_3/J_2 is mathematically equivalent to introducing the Lode angle parameter (e.g. Mohr and Marcadet, 2015).

process in most specimens. Micromechanical simulations are therefore particularly valuable in view of understanding void coalescence.

The first unit cell simulations describing porous microstructures were performed several decades ago (e.g. Tvergaard, 1981), but it is only recently that almost arbitrary loading conditions can be considered for 3D unit cell models. For example, Liu et al. (2016) made use of unit cell simulations with an isotropic power-law matrix material and proportional loading conditions in stress space. They found that at low stress triaxialities, the central void collapses while void coalescence occurs at stress triaxialities above 0.5. They note that void coalescence corresponds to fracture initiation, while the relationship between void collapse and fracture remained unclear. Brüning et al. (2014) describe the fracture process as growth and coalescence of voids and micro-shear cracks. Their unit cell simulations demonstrate that the onset of void coalescence is strongly dependent on the Lode parameter, which is an effect that they incorporated into their latest continuum damage mechanics model. With the help of the results from unit cell simulations, Tvergaard (2015a) discusses the important difference between pure shear and simple shear in the context of ductile failure. For both loading conditions, the stress triaxiality and the Lode parameter are zero, i.e. the hydrostatic part of the stress tensor is zero and the intermediate principal stress equates to the average of the minimum and maximum principal stress. However, localization analysis on single void unit cells reveals that a shear stress maximum can be reached under simple shear (e.g. Tvergaard, 2012), while no localization is predicted under pure shear, even after introducing large imperfections (Tvergaard, 2015a,b). This observation is consistent with the unit cell simulation results of Barsoum and Faleskog (2011) and Dunand and Mohr (2014) who demonstrated the importance of the Lode angle parameter in addition to that of the stress triaxiality as far as coalescence for fixed principal stress directions is concerned. Dunand and Mohr (2014) also repeated their simulations for co-rotational loading conditions, i.e. a loading scenario where the directions of the principal stresses followed the rotation of the central void while keeping the stress state constant. For zero stress triaxiality, the co-rotational loading scenario mimics pure shear conditions, for which, no shear localization has been observed. This remarkable difference between pure shear (no void rotation) and simple shear (active void rotation) suggests that the initial or deformation induced anisotropy of the mechanical system used in the above

simulations plays an important role. The effect of the initial anisotropy can be removed by substituting unit cell simulations through RVE simulations with a random void distribution (e.g. Fritzen et al., 2012). However, to the best of the authors' knowledge, the difference between plastic localization under pure and simple shear has not yet been studied by means of RVE models.

In this work, the governing mechanisms leading to simple shear fracture of an advanced high strength steel sheet material are analyzed through X-ray microtomography (Flannery, 1987) and related synchrotron imaging methods (King, 2008). These methods allow for in-situ damage observations at the sub-micrometer scale, providing unambiguous insight into historically inaccessible damage micro-mechanisms, along with the potential for extremely rich experimental data to enable and validate numerical simulations of real mesostructures. Image-driven three dimensional (3D) structural representations and volumetric measurement of material displacement and/or strain fields at microstructural length-scales allow for the detailed comparison of experimental and simulation results.

Geometrical conditions for sheet material tests cannot readily be met via tomography as only axisymmetric or stick-shape-like specimens can be tested. This shortcoming is overcome by synchrotron laminography (Helfen, 2005). The latter provides an opportunity to monitor in-situ the damage processes in laterally extended sheet-like specimens using physical boundary conditions of engineering relevance (Moffat, 2010, Morgeneyer, 2011). Similar to synchrotron computed tomography, laminography is based on the acquisition of a collection of radiographs of the Region Of Interest (ROI) of the specimen and the subsequent computer-aided reconstruction (Helfen, 2011). X-ray beam directions close to the in-plane directions of the extended specimen are avoided in laminography. Despite the inevitable loss of information and imaging artefacts, laminography is often preferred to tomography where the acquisition angles are limited (Xu, 2012).

The strain fields inside the specimens may be obtained by combining 3D structure imaging during loading with Digital Volume Correlation (DVC). In situ laminography has recently been demonstrated to yield trustworthy measurements at relevant spatial resolutions in the case of alloy tearing (Morgeneyer et al., 2013). DVC is the 3D extension of 2D digital image correlation (e.g. Sutton, 2009), both based on the hypothesis of the conservation of gray levels in 2D or 3D images (Sutton, 2009, Hild

2012). There is a need for ‘natural’ markers, i.e. image contrast, in the material micro- or mesostructure to be able to perform digital volume correlation. A global approach to DVC (Roux, 2008) has been applied to ductile tearing in Morgeneyer et. al. (2013, 2014, 2016). In the global approach, the displacement field parameterization is identical to that used in finite element modeling (Roux, 2008). Mechanical regularization may also be used to help convergence (Taillandier-Thomas et al., 2014). This was performed for Al alloys for which finely dispersed particles or voids with a volume fraction of around 0.3% to 1% served as markers. In steels, the void and particle volume fraction are often even substantially lower so that the natural marker density may be too poor to perform digital volume correlation.

It is the goal of the present work to make use of experiments and computations to reveal the governing mechanism leading to the ductile failure of a polycrystalline multi-phase steel (FB600) under shear-dominant loading conditions. Experiments on smiley-shear specimens are performed in a synchrotron X-ray beam line to monitor the mesostructural evolution through laminography. The role of stiff particles with a diameter of a few micrometers is discussed and the process of void nucleation and growth is analyzed in detail based on the tomography observations and finite element simulations. A computational large deformation analysis of a representative volume element composed of an isotropic elasto-plastic matrix with brittle particles is carried out to replicate the experimental observations and to gain insight into the experimentally-inaccessible final stage of the ductile fracture process.

2. Experimental procedures

A first series of experiments is performed to characterize the macroscopic mechanical response of the sheet material. This involves notched tension, central hole tension and smiley shear experiments. This series of experiments is referred to as “macroscopic experiments” to emphasize that observations are only made at the macroscopic level without any attempt to access stress or strain fields at the mesoscopic or microscopic levels. The latter is the objective of a second series of experiments on smiley shear specimens which we refer to as “tomography experiments”.

2.1. Material

All specimens are extracted from 0.8mm thick sheets of a ferrite-bainite steel (FB600). The main difference between the FB (ferrite-bainite) and conventional DP (dual phase) steels is that it features bainite instead of martensite islands. In a uniaxial tension experiment, the material response is linear up to about 450MPa, followed by positive strain hardening up to a true stress of about 630MPa, where necking sets in. The measured true stress-strain curves (Fig. 1a) show that the material response is direction dependent, with the highest stresses being reached for loading along the transverse direction. The corresponding Lankford ratios are $r_0=0.59$, $r_{45}=1.00$ and $r_{90}=0.90$. Despite its anisotropy, the FB steel is chosen for the current study due to its technological relevance and the presence of dispersed particles that can be easily seen in laminography images. From the point of view of failure mechanism analysis, isotropic steels appear to be more suitable, but given the high plastic strains attained before fracture, even initially isotropic polycrystalline materials are expected to have developed significant plastic anisotropy by the time fracture initiation becomes imminent (e.g. Teodosiu and Hu (1995), Manik et al. (2015)).

2.2. Macroscopic experiments

“Smiley” shear specimens (SH) of 20mm width, containing two parallel shear gage sections (Fig. 2a) have been extracted from the sheet metal using wire-EDM cutting. The exact shape of the gage section (Fig. 2b) had been originally identified for an aluminum AA2198-T8 and is provided in Roth and Mohr (2016). The experiments are performed under displacement control on a 100kN hydraulic universal testing machine (Instron 8801). Custom made high pressure clamps are used to apply the clamping force on the 10mm wide specimen shoulders. All specimens are loaded at 0.4mm/min which results in a strain rate of the order of $10^{-3}/s$ at the gage section level. A random speckle pattern is applied to the specimen surfaces to measure the surface displacement with planar digital image correlation (2D DIC) using the commercial software VIC2D (Correlated Solutions). The images are acquired at a frequency of 1Hz using a digital camera (Point Grey, model GS3-U3-51S5M-C, 2448 x 2048 pixels) with a 1:1 macro lens (Tokina, f2.8, 100mm focal length), resulting in a spatial resolution of 22 μ m/pixel. The first camera’s field of view covers the whole

specimen gage section (approximately 50mm, including the blue dots shown in Fig 2a). A second digital camera (Point Grey, Model GS3-U3-120S6M-C, 4240x2824 pixels) positioned behind the specimen monitored the specimen gage sections with a resolution of $3.1\mu\text{m}/\text{pixel}$.

To identify the plasticity model parameters and to validate the plasticity model for large strains, two additional types of specimen have been tested using the same experimental procedure as for the SH specimen:

- Notched tension (NT20) specimens with a 20mm wide shoulder section and circular cutouts with a notch radius of $R=20\text{mm}$, reducing the width of the gage section to 10mm at the specimen center (Fig. 2c).
- Tension specimens with a central hole (CH). The CH-specimens feature a 20mm wide gage section with a 5mm diameter hole at the center. (Fig. 2d).

2.3. Synchrotron laminography experiments

Experiments on smiley shear specimens are also carried out on beamline ID15A at the European Synchrotron Radiation Facility (ESRF). During the in-situ shear experiments, the loading is applied monotonically through fifteen displacement steps. After each step, a scan (i.e. a series of 3,000 radiographs) is performed with a stationary X-ray beam with the sheet thickness direction being inclined at an angle of 60° with respect to the X-ray beam axis. During each scan, the radiographs are taken while the specimen is rotated around its thickness direction. To perform the rotations around the thickness direction, a custom-made loading frame is mounted onto a motorized stage (Fig. 3). The 3D images used in this work are obtained with a $\sim 60\text{keV}$ white beam. The series of radiographs acquired is then used to reconstruct 3D volumes by using a filtered-back projection algorithm (Myagotin, 2013). The parameter optimization is performed automatically using a GPU-accelerated implementation of this algorithm (Vogelgesang, 2016). The fast GPU implementation is used to automatically optimize reconstruction parameters before processing the data offline. The optimized parameters include the rotation center in the projections and the optimal inclination angles between rotation axis and beam and towards the detector coordinates. The reconstructed volume has a size of $1600 \times 1600 \times 900$ voxels. The physical size (length) of one cubic voxel is equal to $1.095\mu\text{m}$. After scanning the

specimen prior to loading, an additional 14 scans are taken during the step-wise monotonic loading procedure. The last scan corresponds to the fully-opened final crack.

As mentioned in the introduction, a few examples have emerged in the open literature where the strain distribution inside materials can be determined through optical flow techniques. However, the tomography images of the present FB600 material do not exhibit a sufficient density of natural markers for digital volume correlation. As an alternative, we therefore perform planar DIC on projected laminography volumes. For this, all black features present in a $438 \mu\text{m}$ thick slice (being parallel to the specimen mid-plane) are projected on one 2D plane. Subsequently, planar DIC is applied onto the projected images to determine the in-plane components of the strain field. Note that meaningful results are only obtained with this technique under the absence of strain field gradients along the specimen thickness direction.

3. Computational models

Finite element simulations will mainly serve two purposes: firstly, the results from simulations assuming a homogeneous material throughout the gage section are used to estimate the stress state within the shear specimen and to extract the so-called loading paths to fracture, i.e. the evolution of the equivalent plastic strain as a function of the stress triaxiality and the Lode angle parameter. Secondly, simulations are performed to elucidate the effect of stiff particles on the damage evolution within the specimen gage section.

3.1. Finite element model of the shear experiment

The finite element model of the shear experiment comprises a quarter of the SH specimens with an element length of about $l_e = 0.025 \text{ mm}$ and 16 elements over the thickness. Reduced integration first-order solid elements (Abaqus library C3D8R) are used. The experimentally-measured displacement history is applied to the upper boundary of the model. The quasi-static simulation is carried out using the FE code Abaqus/explicit.

To estimate the stress state evolution throughout the shear experiment, the material comprised in the gage section is modeled as a homogenous elasto-plastic solid. In particular, a non-associated quadratic plasticity (Mohr et al., 2010) model with isotropic Swift-Voce hardening is used (green curve in Fig. 1b). Details on the model formulation and model parameter identification from uniaxial tension and notched tension experiments can be found in Roth and Mohr (2014) and Mohr and Marcadet (2015).

3.2. Finite element model of RVE subject to shear-dominant loading

Three-dimensional unit cell models (e.g. Barsoum and Faleskog (2007), Scheyvaerts et al. (2011), Nielsen et al. (2012), Tekoglu et al (2012), Dunand and Mohr (2014)) are usually limited to porous structures of cubic symmetry which may lead to unrealistic predictions of localization events. This problem may be successfully overcome by Representative Volume Element (RVE) models featuring an isotropic void distribution (e.g. Fritzen et al. (2012) used such a model to explore the initial yield response of porous solids). Due to the exceptionally high computational costs associated with the localization analysis with 3D RVE models, a simplified 2D RVE model is employed here. Even though 3D effects are neglected in this model, its predictions are expected to be more realistic than those obtained with 3D unit cell models. Our two-dimensional RVE model consists of about 60,000 first-order plane stress elements with reduced integration (Fig. 4a). Particles of $5\mu\text{m}$ diameter are introduced in the finite element model by finely-meshed circles, being embedded in the matrix material through a hard penalty contact. In the vicinity of the particles, an element length of $l_e = 0.025$ is chosen. The particles are randomly distributed and modeled as purely elastic with a Young's modulus of 184GPa and a Poisson ratio of 0.3. To avoid triggering localization through non-associated plastic flow, the matrix material is modeled as a Levy-von Mises solid with the same hardening behavior as the macroscopic Swift-Voce hardening response (green curve in Fig. 1b). Periodic boundary conditions are applied, while a multiple-point constraint (MPC) subroutine is employed to control the macroscopic stress triaxiality and the direction of the principal stress throughout loading. The RVE simulations are run using the implicit FE-code Abaqus/Standard.

To define the boundary conditions, we introduce the Cartesian frame $(\mathbf{e}_1, \mathbf{e}_2)$ with its origin at the RVE's lower left corner. The undeformed RVE consists of a square with an edge length of $L = 400\mu\text{m}$. The periodic displacement boundary conditions are chosen such that a macroscopic deformation gradient \mathbf{F} of the form

$$\mathbf{F} = F_{11}\mathbf{e}_1 \otimes \mathbf{e}_1 + F_{22}\mathbf{e}_2 \otimes \mathbf{e}_2 + F_{12}\mathbf{e}_1 \otimes \mathbf{e}_2 \quad (1)$$

can be applied. For this, the RVE is deformed by a combination of normal displacements U_i , as well as a tangential displacement U_t in the direction of \mathbf{e}_1 . In matrix notation, we have

$$\mathbf{F} = \begin{bmatrix} 1 + \frac{U_1}{L} & \frac{U_t}{L} \\ 0 & 1 + \frac{U_2}{L} \end{bmatrix}$$

The conditions for the displacements of the nodes situated at the corners of the square read

$$\left\{ \begin{array}{l} u_1(0,0) = 0 \\ u_1(L,0) = U_1 \\ u_1(L,L) = U_t + U_1 \\ \\ u_2(0,0) = 0 \\ u_2(L,0) = 0 \\ u_2(0,L) = U_2 \\ u_2(L,L) = U_2 \end{array} \right. \quad (2)$$

Periodicity is ensured through the conditions

$$\left\{ \begin{array}{l} u_1(L, X_2) - u_1(0, X_2) = U_1 + \frac{U_t}{L} X_2 \\ u_2(L, X_2) - u_2(0, X_2) = \frac{U_2}{L} X_2 \\ u_2(X_1, 0) - u_2(X_1, L) = U_2 \end{array} \right. \quad (3)$$

According to the boundary conditions, the average deformation gradient of the RVE is solely controlled by three degrees of freedom

$$\mathbf{u}(\mathbf{t}) = \{U_1, U_2, U_T\}, \quad (4)$$

which are represented by red arrows in Fig. 4b. Closely following the technical details provided in Section 3.4. of Dunand and Mohr (2014), the macroscopic stress state as

well as the direction of the macroscopic principal stress, which is kept constant, are then controlled through a Multi-Point Constraint (MPC) which is updated after each time increment. The resulting applied histories of the applied displacements are shown in Fig. 4b.

4. Results

4.1. Results from macroscopic shear experiment

Figure 5a shows the experimentally-measured force-displacement curve (black solid dots) for the SH experiment up to the point where the measured force dropped abruptly (the vertical line corresponding to a drop to zero force is not shown; a high speed acquisition system would have been needed to capture this in detail). For ease of discussion, selected instants have been successively labeled from ① to ⑥. The force-displacement curve for the SH-specimen exhibits pronounced work hardening up to the force maximum ④ which is reached at about 90% of the displacement to specimen fracture. Beyond this point, the force level decreases slowly until specimen fracture occurs at instant ⑥.

Detailed pictures of the surface strain fields within the left gage section are shown in Fig. 5b-g for the instants ①, ②, ④ and ⑥ as well as after final fracture. In all contour plots, we show the effective surface strain,

$$\bar{\varepsilon} = \frac{2}{\sqrt{3}} \sqrt{\varepsilon_I^2 + \varepsilon_I \varepsilon_{II} + \varepsilon_{II}^2}, \quad (5)$$

with ε_I and ε_{II} denoting the logarithmic principal strains. As pointed out by Butcher et al. (2017), the effective strain may deviate slightly from the von Mises equivalent strain in case of non-proportional loading paths. As the central (elastically-deforming) part of the specimen moves up, the material in the gage section is subject to large deformation and large rotations. The notches change their shape from a blunt to a sharp notch (e.g. compare notches in Figs. 5b and 5e). At the same time, a hypothetical line connecting the notch roots, rotates counterclockwise by about 24° , changing the angle from about $+10^\circ$ (in Fig. 5b) to -14° (Fig. 5e) with respect to the vertical axis. After the force maximum (instant ④), the degree of concentration of

plastic deformation within the gage section increases substantially. At instant ④, the width of the red band in the strain contour (i.e. the region where the effective strain exceeds 90% of the maximum value) is only about $120\mu\text{m}$ wide. With a subset size of 15 pixels and a step size of 5 pixels, the computed effective strain at this point is about $\bar{\epsilon} = 1.4$.

Upon close examination of the DIC pictures, small cracks are first detected at instant ④ on the notched gage section boundary (as highlighted by white arrows in Fig. 5b). The cracks grow in a stable manner before total specimen failure is observed at instant ⑥. The final crack path lies within the zone of highest effective strain that has been observed at instant ⑥. Given that the stress state at a free boundary cannot be pure shear (i.e. the free boundary condition $\sigma\mathbf{n} = \mathbf{0}$ cannot be satisfied by a stress tensor of the form $\sigma = \tau(\mathbf{t} \otimes \mathbf{s} + \mathbf{s} \otimes \mathbf{t})$), the strains achieved at instant ④ cannot be interpreted as fracture strains for pure shear. However, the effective strain achieved at the specimen center at instant ⑥ may be interpreted as a lower bound for the fracture strain under shear loading.

4.2. Results from numerical simulation of the fracture experiments

Table 1 summarizes the identified plasticity model parameters for the FB600 steel. The numerical simulations for notched tension and central hole tension are in good agreement with the experiments as far as the global force-displacement response and surface strain fields are concerned (Fig. 6), thereby partially confirming the validity of the phenomenological plasticity model. The numerical simulation of the SH experiment (solid line in Fig. 5a) had been stopped at instant ④; the occurrence of cracks in the experiments between points ④ and ⑥ would make the comparison with a crack-free simulation invalid.

The good agreement of the strain contour plots in Fig. 7 (simulations) with the corresponding experimental results (Fig. 5b) provides additional support for the choice of the plasticity model as far as the estimation of the mechanical fields within the specimen gage section is concerned. The detailed comparison of the experimentally-measured and numerically-predicted strain fields reveals local differences of less than 5%. It is noted that the effective strain had been defined as user-defined output variable in the FE model to ensure the comparability of the

experimental and numerical results. The evolution of the stress triaxiality fields within the specimen gage section is shown by the right column contour plots in Fig. 7. For each instant, the stress triaxiality contour is shown for the specimen surface ($z = \pm t/2$), the mid-plane ($z = 0$) and for the quarter plane ($z = \pm t/4$). On the specimen surface, the stress triaxiality is very close to 0 throughout the entire gage section. However, at the gage section boundaries, non-zero stress triaxialities are observed. In particular, we observe a tensile zone within which the triaxiality reaches values of up to 0.58 near the mid-plane. The comparison of the triaxiality fields on the specimen surface and mid-plane also reveals that a through-thickness gradient in stress triaxiality builds up throughout the experiment. To elucidate this effect, we plotted the evolution of the stress triaxiality as a function of the equivalent plastic strain for all sixteen elements located at the specimen center (Fig. 8a). While a maximum stress triaxiality of 0.11 is reached on the specimen surface, a maximum of 0.35 is reached on the specimen mid-plane. In terms of the Lode angle parameter, we have a maximum of $\bar{\theta} = 0.36$ on the specimen surface, and $\bar{\theta} = 0.56$ on the specimen mid-plane (Fig. 8b). For reference, we also show the evolution of the stress state for the material point, at which the highest equivalent plastic strain had been reached in the simulation of the SH, CH and NT20 experiments (Figs. 8c and 8d).

4.3. Results from laminography experiments

Figure 9a shows a representative $1.095\mu\text{m}$ thick (i.e. one voxel in thickness direction) slice of the undeformed specimen, while Fig. 9b shows a projection of the gray value minima over a thickness of $438\mu\text{m}$. The black voxels indicate lower density matter which was identified as CaO particles by Kahziz (2015). The volume fraction of particles greater than $1\mu\text{m}$ (smaller particles are not detected with the current laminography set-up) is 0.015%. The average particle size seen in the laminography images is about $5\mu\text{m}$.

4.3.1 Strain estimates via planar DIC on projected laminography volumes

The force-displacement curve recorded during the laminography SH-experiment (red cross symbols in Fig. 5a) coincides with those determined from repeated macroscopic experiments. Figure 10 shows the effective strain fields that are obtained

from planar DIC on 2D projections of a $438\mu\text{m}$ thick stack of laminography slices located at the specimen mid-plane. The region close to the notched boundary has been excluded due to the development of non-negligible through thickness gradients in the strain field. The comparison with the surface strain fields measured in the macroscopic experiments reveals that the shape and magnitude of the strain field are consistent with the surface measurements and also with the simulations, thereby validating all three approaches for this material and specimen geometry. The effective strain to fracture as identified through planar DIC on projected laminography images is $\bar{\epsilon} = 1.5$ near the specimen center.

Figure 11 shows the strain profiles for instances ①, ②, ④ and ⑥ along the line indicated in Fig 10a as extracted from (i) the simulation, (ii) the surface DIC measurement, and (iii) the correlation of laminography projections. Good agreement is found for the experimental methods (red and blue curves), while the numerical simulation (blue dots) slightly overestimates the amount of strain. As far as the width of the deformed zone is concerned, similar results are obtained for all three methods.

4.3.2 Void evolution under shear-dominated loading

Figure 12 shows laminography images of the specimen mid-plane for the time instants highlighted on the force-displacement curves shown in Fig. 5a. Projected images are shown for a $17\mu\text{m}$ thick slice to ensure that full particles are included in the images. The last pictures before total specimen fracture (instants ④-⑥) confirm that small cracks form at the notched gage section boundaries. The picture of the undeformed specimen (Fig. 12a) shows a circular notch with surface roughness of less than $5\mu\text{m}$. However, throughout the entire loading history the notch shape evolves significantly, changing from round to blunt. At the same time, the notch roots move in opposite directions along the horizontal axis. This evolution could already be seen in the macroscopic pictures. However, the laminography pictures also reveal that the surface roughness increases gradually, with up to $8\mu\text{m}$ deep dents at instant ②. One of the dents at the lower notch eventually begins to grow deeper into the gage section (Fig. 12d, instant ③), generating a crack-like trace in the subsequent pictures. The total length of this apparent crack is about $65\mu\text{m}$ in the last picture before total specimen failure (Fig. 12f, instant ⑥).

To study the mesostructural deformation mechanism near the specimen center, we focus on a group of three particles that are located inside the narrow zone of high plastic deformation (see region inside the white rectangles in Fig. 12). The corresponding sequence of magnified images is shown in Fig. 13. The main observations are:

1. In the initial configuration prior to mechanical loading (Fig. 13a), we observe round particles of about $5\mu\text{m}$ diameter with a particle-to-particle distance greater than $100\mu\text{m}$.
2. After loading the material up to an effective strain of up to 0.65 at the macroscopic level (instant ①, Fig. 13b), we can see that the initially round black areas become approximately elliptical with their major axis being inclined at an angle of about 51° with respect to the horizontal direction. Incidentally, this direction coincides with that of the maximum principal strain in the finite elements simulations. The particle-to-particle distance has also decreased and the hypothetical connecting lines rotated counter-clockwise, which is due to the simple shear kinematics. Assuming that the particles undergo only small elastic deformation, the shape and size change of the black areas is attributed to void nucleation through matrix-particle decohesion.
3. Up to the maximum force (instant ④, Fig. 13e), the voids continue to grow along their major axis. With respect to the horizontal direction it is inclined at an angle of 54° at instant ② and up to 69° at instant ④. The void width remains constant which is tentatively attributed to the presence of a stiff particle.
4. After the force maximum (instants ⑤ and ⑥, Fig. 13f), blunt cracks are growing from the voids into the matrix. The crack direction is different from the principal axis of the voids and appears to approach the direction of macroscopic shear loading (vertical axis).

Note that Fig. 13f is the last image that we were able to record prior to specimen fracture.

To provide a three-dimensional view of the damage evolution under shear dominated loading, we consider a $440\mu\text{m}$ thick slice around the specimen mid-plane

(Fig. 14). The dense metal matrix is made transparent here, while the less dense particles and voids are shown in blue. Note that the laminography system cannot differentiate between particles and voids. In the first image (Fig. 14a), all blue areas correspond to existing particles with the initial porosity being negligible compared to the particle density. This has been verified with the help of energy dispersive X-ray spectroscopy (EDS) during scanning electron microscopy where it was possible to differentiate between CaO particles and void space. Since the particles are only subject to small elastic strains, the increase in the volume fraction of the blue phase from Figs. 14a to 14d is attributed to the nucleation and growth of voids between the particles and the matrix material. Most of the void growth and rotation is found in the shear zone which is consistent with the increased plastic strain in this area. Voids have sharp edges at their ends and are round in the middle, which supports the assumption that the particles are deforming elastically only. The longest axis of the elongated voids is not completely parallel to the final fracture plane. While the features seen in the top views just confirm the observations made when monitoring a group of particles only, the views normal to the plane of fracture in Fig. 14 reveal a new feature. After loading, the voids are not only extended along the direction of loading, but also along the specimen thickness direction. This observation suggests that the voids develop flat crack like features with narrow ends.

To confirm this observation, post-mortem fractography is carried out on the final fracture surface of the observed crack. Typical large dimples that formed in the central shear zone are highlighted in Fig. 15a. They result from the first population of voids that nucleated around CaO particles, and which were sufficiently large to be seen by laminography. The magnified detail view in Fig. 15b shows a large dimple containing a particle. It can be seen that this dimple is particularly flat compared to typical voids grown in crack tip fields at high stress triaxialities. The areas between large dimples are either flat or covered with sub-micrometer sized dimples. The latter are associated with the void sheeting mechanism. For the present alloy it is likely that a second population of much smaller micro-voids has nucleated at ferrite-bainite interfaces. The interpretation of the origin of the flat areas is more challenging. A first scenario is that these were also populated by micro-dimples which got smeared out due to inevitable contact between opposing fracture surfaces. A second scenario is

transgranular fracture which cannot be excluded based on our experimental observations.

To gain further insight into void evolution, the combined particle and void volume fraction has been measured in $55\mu\text{m}$ thick slices. The initial void volume fraction as well as the void volume fraction evolution are shown in Fig. 16. The initial particle volume fraction is around 0.015%. Just before failure, the void volume fraction is at about $0.065-0.015=0.05\%$ in the shear zone. The following representative volume element (RVE) analysis strongly supports the speculation that the hard CaO particles in the ferrite matrix material act as triggers of shear localization at the mesostructural level.

4.4. Scenarios leading to final specimen failure

The final stage of the specimen failure, i.e. the fracturing of the specimen into two parts, could not be observed in the tomography experiments. With the present laminography technique, the scanning time for a single image exceeds by far the duration of the final fracture event. Based on the current experimental evidence, two scenarios appear to be realistic:

- Fracture scenario #1 – change from stable-to-unstable growth of the corner cracks: As mentioned above, two cracks form in the tensile region of the notched boundaries at instant (4), well before the total specimen fracture. These cracks grow in a stable manner up to the instant (6). A first speculation would be to assume that the growth of these cracks becomes unstable at instant (6), explaining the final separation of the specimen by the unstable propagation of the corner cracks.
- Fracture scenario #2 – nucleation of an unstable crack due to shear-induced damage. Figure 14c shows approximately uniform damage along the path of the final crack. In case the condition for crack initiation is met at one location, it is expected that the crack will immediately propagate in an unstable manner since the conditions are expected to be equally-critical throughout the entire gage section.

4.5. Results from RVE analysis

We analyze the response of an RVE under remote shear straining to assess whether the type of shear damage observed in the experiments could potentially lead to ductile fracture (scenario #2). Figure 17 shows the results from the analysis of the deformation response of an RVE with randomly-distributed particles. The initial particle density in the computational model is 0.015% which matches the experimentally-measured value. The stress-triaxiality evolves according to the loading path to fracture at the location of maximum equivalent plastic strain in the global FEA of the SH experiment (path labeled “SH” in Fig. 8c). This location on the specimen mid-plane (its in-plane position is highlighted in Fig. 7e) is close to the area of interest chosen for the detailed laminography analysis (compare with white rectangle shown in Fig. 12e). In a first approximation, the direction of the principal stress is kept constant (it decreases from about 50° to 37° in the global FEA). In Fig. 17b, a white arrow indicates the orientation of the maximum principal stress at the macroscopic level. For an isotropic material, this orientation corresponds to the direction of the maximum principal strain. Due to the assumption of zero particle-matrix interface strength, the matrix already detaches from the particle at an early stage of deformation. Two cavities grow in the direction of the maximum principal strain. The contour plots nicely illustrate that the presence of the particle prevents the collapse of the void, i.e. compressive stresses build up in the contact areas between the particle and the matrix.

The plot of the evolution of the total strain energy (sum of elastic strain energy and plastic dissipation) in Fig. 17f shows a decrease as the applied deformation increases from configuration (b) to (e). Given the irreversibility of the plastic part, this decrease corresponds to a decrease in the elastic strain energy. In other words, a portion of the material comprised in the RVE experiences elastic unloading. When comparing the strain fields given by Figs. 17d and 17e, it is clearly visible that the plastic deformation increases only within a band of the width of the particle diameter, while the plastic deformation in the material outside that band remains unchanged. Knowing that the matrix material exhibits positive strain hardening only (matrix softening is excluded), it is clear that the elastic strain energy within the band of localized deformation must continue to increase between stages (d) and (e). Conversely, it is clear that the material outside the band is elastically unloaded. We

therefore conclude that the band seen in Fig. 17e is not just a band of concentrated plastic deformation, but it is a strain localization band (“shear band” in a wide sense) whose emergence is accompanied by the elastic unloading of the surrounding material. We also note that the observed decrease in strain energy corresponds to softening of the effective response of the RVE and hence a possible loss of ellipticity. However, the above observations may also be interpreted as a sub-cell localization phenomenon (see recent literature on void coalescence, e.g. Benzerga and Leblond (2014), Benzerga et al. (2016), Torki et al. (2017)), in which case classical localization theory (e.g. Mandel (1966), Rice (1976)) may no longer be adequate. Different from unit cell analyses, the plane of localization is not pre-set by the periodic boundary conditions in case of an RVE. In the present simulations, the band of localized deformation emerges naturally at an angle of about 45° with respect to the direction of the maximum principal stress. In other words, the orientation of the emerging localization band coincides with the direction of maximum shear. This observation is roughly in line with the results of theoretical localization analysis (e.g. Forest et al., 2005), which suggest that the plane of localization in an isotropic elastoplastic solid is aligned with the direction of maximum shear in case the eigenvalues of the plastic flow direction (here at the macroscopic level) are identical, but of opposite sign (i.e. pure shear kinematics). As the elastic strain energy decreases further, the shear localization bands developing at neighboring particles begin to interact which results in an S-shaped band of localization between particles. After the formation of bands of highly localized plastic deformation, a crack is expected to form inside these bands in a void sheet mechanism, whose traces had been observed in the post-mortem SEM images.

The result from the above RVE analysis is important as it shows that shear band type of failure is possible when subjecting a von Mises solid containing a low volume fraction ($\ll 0.1\%$) of stiff particles to shear-dominant loading. Note that no shear localization would be found (at reasonable strain levels) in a Levy-von Mises solid without any particles.

Comment regarding the model reliability: It is difficult to verify the reliability of the finite element solution. To rule out that mesh artifacts led to shear localization, we also repeated the above RVE simulation using the same mesh (with particle features), but we assigned the same material card to the particles and matrix, and assumed

perfect particle-matrix adhesion (tie contact). As expected from theoretical considerations, no shear localization was found in that computational analysis. The assumption of zero particle-matrix interface strength, allowed us to reach the point of shear localization at strains that did not exceed the strain levels observed in the simulations of the notched tension, central hole tension and shear experiments. The good agreement of simulations and experiments for the latter is therefore also seen as a partial validation of the finite element modeling framework employed for the RVE analysis. Given the large shear strains involved, we also performed a single element simulation for simple shear to quantify the Swift-Poynting effect. When using the Abaqus/implicit solver in conjunction with the J2-plasticity model, the normal stresses under pure shear remain close to zero, even at equivalent plastic strains of 2. We also note that more than 200 implicit time steps have been performed to minimize errors related to the incremental linearization of the kinematics of finite strain.

4.6. Results from full specimen analysis with stiff particles

The RVE analysis provides a physically-sound explanation of ductile fracture initiation under remotely applied shear. Here, we repeat the simulations of the shear experiments using a 2D mesh with elastic particles to demonstrate that the strain localization observed for remote straining can also occur for the exact boundary conditions in our experiments.

The corresponding finite element mesh (Fig. 18a) features 1.3 million first-order plane stress elements (CPS4R from Abaqus library). It includes ten quasi-randomly distributed rigid particles of $5\mu\text{m}$ diameter, which corresponds to a particle volume fraction of about 0.015% within the gage section. The exact position of the particles within the gage section is chosen in accordance with the large particles seen in the tomography image of the mid-plane (Figs. 12a and 13a). Recall that Fig. 12 is a projected image for a $17\mu\text{m}$ thick slice, and hence the apparent particle area density is higher than that seen in the 2D FE-mesh. As in the RVE model, zero strength is assumed for the particle-matrix interface. The same type of boundary conditions as in the previous homogeneous model of the shear experiment are applied. The numerical simulation is performed using Abaqus/explicit with approximately 1.28 million explicit time increments. It was executed in double precision on a high performance cluster in MP-mode with 24 CPUs in parallel.

A sequence of equivalent plastic strain contour plots is shown in Figs. 18e to 18i. As in the macroscopic model, we observe a first strain concentration at the notch roots. The deformation around the particles evolves in a manner that is very similar to the RVE simulations. The most important aspect of the results from the detailed 2D simulation is that a band of localized deformation forms between two neighboring particles at the mesoscale (Fig. 18h,m), inside the macroscopic band of concentrated shear deformation. Clearly, this type of localization would be absent in a homogeneous material without any particles. The simulation model is not set up for predicting fracture. Therefore, we still cannot judge from the present simulations whether the total specimen failure is due to propagating corner cracks or fracture initiation within the gage section due to shear damage. However, we can confirm that the shear failure mechanism inferred from the RVE simulations is not only possible for idealized remote straining boundary conditions, but it is also possible when the material is subjected to the actual boundary conditions of a real shear experiment.

4.7. Discussion

Based on the experimental and numerical results, the mechanism leading to fracture initiation under shear-dominant loading conditions is summarized as follows:

1. Shear damage phase (observed experimentally) (Fig. 19a-b):
 - a. Void nucleation due to particle-matrix decohesion.
 - b. Void growth around the stiff particles after decohesion. During the growth phase, the major principal axis of the void is aligned with the direction of the maximum principal strain.
 - c. Formation of highly elongated voids with micro crack-like features. For particles of $5\mu\text{m}$ diameter, we observe up to $25\mu\text{m}$ long micro-cracks on either side of the particles. As for the growing voids, the major axis of the micro-crack like features is parallel to the direction of the principal strain.
2. Formation of a mesoscopic localization band (only observed in the RVE model): The volume fraction of porous space due to shear-damage is very small since it takes place under nearly isochoric conditions. The estimated maximum void volume fraction before macroscopic fracture initiation is only

0.05%. However, as shown through RVE analysis, a very small void volume fraction is sufficient to meet the conditions for the formation of a band of localized plastic deformation within a RVE with zero particle-matrix interface strength. The RVE simulations suggest that the orientation of the mesoscopic localization bands is initially close to the direction of maximum shear (Fig. 19c-d).

3. Formation of a macroscopic crack (speculation): inside the mesoscopic bands of localized plastic deformation, additional voids are expected to nucleate at a smaller length scale, leading to the formation of a crack through a void sheet mechanism (traces of which have been observed in the post-mortem SEM images).

Many elements of the postulated fracture mechanism are not new. Similar observations and analyses can be found in the open literature, but for higher stress triaxialities only (e.g. Weck and Wilkinson (2008), Morgeneyer et al. (2014), Ueda et al. (2014)). What is new is the direct experimental observation of the above damage mechanism for shear-dominant loading conditions and the numerical demonstration that this type of shear damage may potentially lead to ductile failure. This has only been possible by combining recent progress in shear fracture testing (e.g. the development of the smiley specimen by Roth and Mohr (2016)) with in-situ monitoring through laminography. The importance of the obtained results becomes more apparent when considering the fact that void growth under shear cannot be explained through basic micromechanical considerations due to the absence of a hydrostatic driving force.

An interesting aspect of the results from the mesoscopic simulations is that the orientation of the final crack is neither perpendicular to the direction of the maximum principal stress, nor does it coincide with the direction of damage-related micro-cracks. The apparent micro-cracks are the outcome of void growth around the stiff particles. Their orientation is therefore parallel to the direction of maximum principal strain, i.e. the direction of void growth. However, the plane of localized plastic deformation is initially inclined at an angle of about 45° with respect to the direction of the maximum principal stress.

It is reemphasized that the experimental observations exclude the final stage of the ductile fracture process. The time scale associated with the transition from the shear damage phase to a final crack is too short for the employed laminography technique. Tentative conclusions with regards to the final shear fracture mechanism are mostly based on finite element simulations. Due to the uncertainty related to the modeling assumptions made, it is important to reconfirm the present conclusions through additional experimental observations once suitable high speed imaging techniques become available. Further optimization of the shape of the shear specimen might also help in generating even stronger experimental evidence on shear fracture. Firstly, it might be possible to identify a specimen shape that will prevent the initiation of tensile cracks near the notch boundaries. Secondly, an optimized shape might also reduce the growing deviation of the stress state from pure shear ($\eta = 0, \bar{\theta} = 0$) as the specimen deforms plastically. Based on the results from localization analysis (e.g. Mohr and Dunand, 2014), the development of positive stress triaxialities is expected to favor fracture initiation, while the development of non-zero Lode parameter values is expected to delay fracture initiation.

There are two potentially-important qualitative aspects that our basic elasto-plastic simulations cannot capture: firstly, the evolution of the surface roughness of the notched boundaries cannot be described. It is expected to play an important role during the crack initiation from the notches. For example, the strains at the instant of corner crack initiation under tension in the SH specimen (about 0.92) are lower than the strains at the instant of crack initiation in the CH specimens (about 1.17). Research on edge fracture (e.g. Wang and Wierzbicki, 2014) has shown the first-order effect of the edge condition on the fracture strains in DP steels. The second apparent shortcoming of our simulations is their inability to predict the exact shape of the voids. The simulated shape is different from the elongated crack-like voids in the tomography pictures (compare Figs. 17n and 13f). Given that the nucleation of a void may be seen as the creation of an internal free boundary, we expect that the same mechanism leading to a substantial simulation/experiment difference in the notched boundary roughness, is also responsible for the poor agreement in void shape.

And finally, it is also reemphasized that the present observations were made for a ferrite-bainite steel FB600. As discussed by Papasidero et al. (2014), general

conclusions must be drawn with care since ductile fracture mechanisms can be material dependent.

5. Conclusions

Advanced porous plasticity models account for the elongation and rotation of voids, thereby providing a physically-sound micromechanical basis for predicting ductile fracture under shear-dominant loading conditions. Here, an attempt is made to prove experimentally that ductile damage indeed nucleates and grows when a real engineering material is subject to remote shear. For this, two recently-developed experimental techniques are combined: due to the progress in laminography (e.g. Helfen et al., 2005), mesostructural features in polycrystalline sheet materials can now be observed with a resolution of a few micrometers. At the same time, the development of a compact shear specimens (e.g. Roth and Mohr, 2016) makes it possible to perform a simple shear experiment on a gage section that is sufficiently small for in-situ laminography on a synchrotron X-ray beam line.

It has been postulated in the experimental literature that the ductile fracture mechanism changes from (some undefined) shear-dominated fracture mechanism to fracture due to void formation as the stress triaxiality increases (e.g. Bao and Wierzbicki, 2004). The present laminographic observations show that voids do form inside a 0.8mm thick ferritic-bainitic steel (FB 600) when the material is subject to a simple shear type of loading, thereby providing strong experimental support of the modeling assumptions of advanced GTN type of models (e.g. Malcher et al. (2014), Morin et al. (2016)). Due to the presence of CaO particles, voids nucleate by particle-matrix interface failure, grow and develop into micro-cracks throughout the monotonic shear experiment. Detailed finite element analysis of a representative volume element subject to remote shear suggests that a low volume fraction of particles (0.015% in the present case) is already sufficient to trigger the formation of shear-band type of failure at the mesoscopic level. The developed void volume fraction is very low (less than 0.1% in the last measurement before specimen fracture) and unlikely to be detected as dilatant plastic flow at the macroscopic level. The reported ductile failure mechanism is well-known for high stress triaxialities, going back to the seminal works on ductile fracture in the 1970's. However, due to the high

complexity of shear fracture experiments and the associated localization analysis, it is only now that this mechanism has also been clearly demonstrated for shear-dominated loading conditions.

Acknowledgements

ArcelorMittal is gratefully acknowledged for supplying the FB600 material. The European Synchrotron (ESRF) beamline ID15 is thanked for providing beamtime (experiment me1366).

References

- Abaqus, Reference manuals v6.12-3, Abaqus Inc, 2012.
- Altenbach, H., 1994. *Kontinuumsmechanik: Einführung in die materialunabhängigen und materialabhängigen Gleichungen*, Teubner, Stuttgart.
- Argon, A. S., 1976. Formation of Cavities from Nondeformable Second-Phase Particles in Low Temperature Ductile Fracture. *Journal of Engineering Materials and Technology* 18, 60–68.
- Baczmanski, A., Zhao, Y., Gadalinska, E., Le Joncour, L., Wronski, S., Braham, C., Panicaud, B., Francois, M., Buslaps, T., Soloducha, K., 2016. Elastoplastic deformation and damage process in duplex stainless steels studied using synchrotron and neutron diffractions in comparison with a self-consistent model. *International Journal of Plasticity* 81, 102–122.
- Bao, Y., Wierzbicki, T., 2004. On fracture locus in the equivalent strain and stress triaxiality space, *Int. J. Mech. Sciences*, 46, 81–98.
- Barsoum, I., Faleskog, J., 2007. Rupture mechanisms in combined tension and shear—Micromechanics, *International Journal of Solids and Structures* 44 (17), 5481-5498.
- Barsoum, I., Faleskog, J., 2011. Micromechanical analysis on the influence of the Lode parameter on void growth and coalescence. *International Journal of Solids and Structures* 48, 925-938.
- Benzerga, A.A., Besson, J., 2001. Plastic potentials for anisotropic porous solids. *European Journal of Mechanics - A/Solids* 20 (3), 397-434.
- Benzerga, A.A., Leblond, J.B., 2010. Ductile fracture by void growth to coalescence. *Adv. Appl. Mech.* 44, 169-305.
- Benzerga, A.A., Leblond, J.B., 2014. Effective Yield Criterion Accounting for Microvoid Coalescence. *Journal of Applied Mechanics* 81 (3), 031009.
- Benzerga, A.A., Leblond, J.B., Needleman, A., Tveergaard, V., 2016. Ductile Failure Modeling. *International Journal of Fracture* 201(1), 29–80.
- Brüning, M., Gerke, S., Hagenbrock, V., 2014. Stress-state-dependence of damage strain rate tensors caused by growth and coalescence of micro-defects. *International Journal of Plasticity* 63, 49–63.
- Butcher, C., Abedini, A. 2017. Shear Confusion: Identification of the Appropriate Equivalent Strain in Simple Shear using the Logarithmic Strain Measure. *International Journal of Mechanical Sciences* 134, 273-283.
- Chu, CC, Needleman AA, 1980. Void Nucleation Effects in Biaxially Stretched Sheets. *ASME J. Eng. Mater. Technol.* 102(3), 249-256.
- Daehli, B., Borvik, T., Hopperstad, O.S., 2016. Influence of loading path on ductile fracture of tensile specimens made from aluminium alloys. *International Journal of Solids and Structures* 88–89, 17–34.
- Danas, K., Ponte Castañeda, P., 2012. Influence of the Lode parameter and the stress triaxiality on the failure of elasto-plastic porous materials, *International Journal of Solids and Structures* 49 (11–12), 1325-1342.
- de Geus, T.W.J., Peerlings, R.H.J., Geers, M.G.D., 2016. Competing damage mechanisms in a two-phase microstructure: How microstructure and loading

- conditions determine the onset of fracture. *International Journal of Solids and Structures* 97_98, 687–698.
- Dunand, M., Mohr, D., 2010. Hybrid experimental–numerical analysis of basic ductile fracture experiments for sheet metals. *Int. J. Solids and Structures* 47(9), 1130–1143.
- Dunand, M., Mohr, D., 2014. Effect of Lode parameter on plastic flow localization after proportional loading at low stress triaxialities. *J. Mech. Phys. Solids* 66, 133–153.
- Flannery, B.P., Deckman, H.W., Roberge, W.G., D'Amico, K.L., 1987. Three-Dimensional Microtomography. *Science* 237, 1439–1444.
- Fleck, N.A., Hutchinson, J.W., Tvergaard, V., 1989. Softening by Void Nucleation and Growth in Tension and Shear. *J. Mech. Phys. Solids* 37, 515–540.
- Forest, S., Blazy, J.-S., Chastel, Y., Moussy, F., 2005. Continuum modeling of strain localization phenomena in metallic foams. *Journal of Materials Science* 40, 5903–5910.
- Fritzen, F., Forest, S., Böhlke, T., Kondo, D., Kanit, T., 2012. Computational homogenization of elasto-plastic porous metals, *Int. J. Plast.* 29, 102–119.
- Ghahremaninezhad, A., Ravi-Chandar, K., 2012. Deformation and failure in nodular cast iron. *Acta Mater.* 60, 2359–2368.
- Gologanu, M., Leblond, J.-B., Devaux, J., 1993. Approximate models for ductile metals containing non-spherical voids—case of axisymmetric prolate ellipsoidal cavities. *Journal of the Mechanics and Physics of Solids* 41 (11), 1723–1754.
- Gurson, A. L., 1977. Continuum Theory of Ductile Rupture by Void Nucleation and Growth: Part I – Yield Criteria and Flow Rules for Porous Ductile Media. *Journal of Engineering Materials and Technology* 99, 2–15.
- Helfen, L., Baumbach, T., Mikulík, P., Kiel, D., Pernot, P., Cloetens, P., Baruchel, J., 2005. High-resolution three-dimensional imaging of flat objects by synchrotron-radiation computed laminography. *Appl. Phys. Lett.* 86 (7), 071915.
- Helfen, L., Myagotin, A., Mikulík, P., Pernot, P., Voropaev, A., Elyyan, M., Di Michiel, M., Baruchel, J., Baumbach, T., 2011. On the implementation of computed laminography using synchrotron radiation. *Rev. Sci. Instrum.* 82, 063702.
- Hild, F., Roux, S., 2012. Digital Image Correlation, in: Rastogi, P.K., Hack, E. (Eds.), *Optical Methods for Solid Mechanics: A Full-Field Approach*, Wiley, Weinheim, pp. 183–228.
- Hill, R., 1948. A theory of the yielding and plastic flow of anisotropic metals. *Proceedings of the Royal Society of London Series A* 193, 281–297.
- Horstemeyer, M.F., Lathrop, J., Gokhale, A.M., Dighe, M., 2000. Modeling stress state dependent damage evolution in a cast AlSiMg aluminum alloy. *Theor. Appl. Fract. Mech.* 33, 31–47.
- Horstemeyer, M.F., Matalanis, M.M., Sieber, A.M., Botos, M.L., 2000. Micro-mechanical finite element calculations of temperature and void configuration effects on void growth and coalescence. *Int. J. Plast.* 16, 979–1015.
- Kahziz, M., 2015. Étude expérimentale et numérique des mécanismes d'endommagement ductile et rupture des bords découpés des aciers avancés pour l'automobile, PhD thesis, Mines ParisTech

- Kahziz, M., Morgeneyer, T. F., Maziere, M., Helfen, L., Maire, E., Bouaziz, O., 2016. In-situ 3-D synchrotron laminography assessment of edge fracture in DP steels: quantitative and numerical analysis. *Experimental Mechanics* 56, 177-195.
- Keralavarma, S.M., Benzerga, A., 2008. An approximate yield criterion for anisotropic porous media, *C.R. Mecanique*, 336, 685-692.
- Khadyko, M., Marioaram C. D., Ringdalen, I. G., Dumoulin, S., Hopperstad, O. S., 2016. Deformation and strain localization in polycrystals with plastically heterogeneous grains. *International Journal of Plasticity* 86, 128–150.
- Khan, I.A., Bhasin, V., 2017. On the role of secondary voids and their distribution in the mechanism of void growth and coalescence in porous plastic solids. *International Journal of Solids and Structures* 108, 203–215.
- Kim, J.B., Yoon, J.W., 2014. Necking behavior of AA 6022-T4 based on the crystal plasticity and damage models. *International Journal of Plasticity* 73, 3–23.
- King, A., Johnson, G., Engelberg, D., Ludwig, W., Marrow, J., 2008. Observations of Intergranular Stress Corrosion Cracking in a Grain-Mapped Polycrystal. *Science* 321(5887), 382-385.
- Lee, J., Kim, J. H., Lee, M. G., Barlat, F., Zhou, C., Chen, Z., Wagoner, R. H., 2015. Properties controlling the bend-assisted fracture of AHSS. *International Journal of Plasticity* 75, 100–120.
- Ling, C., Besson, J., Forest, S., Tanguy, B., Latourte, F., Busso, E., 2016. An elasto-viscoplastic model for porous single crystals at finite strains and its assessment based on unit cell simulations. *International Journal of Plasticity* 84, 58–87.
- Liu, Z.G., Wong, W.H., Guo, T.F., 2016. Void behaviors from low to high triaxialities: Transition from void collapse to void coalescence. *International Journal of Plasticity* 84, 183–202.
- Madou, K., Leblond, J.B., 2012. A Gurson-type criterion for porous ductile solids containing arbitrary ellipsoidal voids – I: limit-analysis of some representative cell. *J. Mech. Phys. Solids* 60, 1020-1036.
- Malcher, L., Andrade Pires, F.M., César de Sá, J.M.A., 2014. An extended GTN model for ductile fracture under high and low stress triaxiality. *International Journal of Plasticity* 54, 193-228.
- Mandel, J., 1966. Conditions de stabilite et postulat de Drucker, in : Kravtchenko, J., Sriyes, P.M., *Rheology and Soil Mechanics*, Springer, Berlin, pp.58.
- Mánik, T., Holmedal, B., Hopperstad, O.S., 2015. Strain-path change induced transients in flow stress, work hardening and r-values in aluminum. *International Journal of Plasticity* 69, 1-20.
- Marcadet, S.J., Mohr, D., 2015. Effect of compression-tension loading reversal on the strain to fracture of dual phase steel sheets. *Int. J. Plast.* 72, 21-43.
- Matsuno, T., Teodosiu, C., Maeda, D., Uenishi, A., 2015. Mesoscale simulation of the early evolution of ductile fracture in dual-phase steels. *International Journal of Plasticity*, 74, pp.17–34.
- McClintock, F.A., 1968. A Criterion for Ductile Fracture by the Growth of Holes. *ASME. J. Appl. Mech.* 35(2), 363-371.
- Mohr, D., Treitler, R., 2008. Onset of fracture in high pressure die casting aluminum alloys. *Eng. Fract. Mech.* 75, 97–116.

- Mohr, D., Dunand, M., Kim, K.H., 2010. Evaluation of associated and non-associated quadratic plasticity models for advanced high strength steel sheets under multi-axial loading. *Int. J. Plasticity* 26(7), 939-956.
- Mohr, D., Marcadet, S.J., 2015. Micromechanically-motivated Phenomenological Hosford-Coulomb Model for Predicting Ductile Fracture Initiation at Low Stress Triaxialities. *Int. J. Solids and Structures* 67–68, 40–55.
- Moffat, A.J., Wright, P., Helfen, L., Baumbach, T., Johnson, G., Spearing, S.M., Sinclair, I., 2010. In situ synchrotron computed laminography of damage in carbon fibre-epoxy [90/0]s laminates. *Scripta Mat.* 62, 97-100.
- Morgeneyer, T.F., Besson, J., 2011. Flat to slant ductile fracture transition: tomography examination and simulations using shear controlled void nucleation. *Scripta Mat.* 65, 1002-1005.
- Morgeneyer, T.F., Helfen, L., Mubarak, H., Hild, F., 2013. 3D Digital Volume Correlation of Synchrotron Radiation Laminography images of ductile crack initiation: An initial feasibility study. *Exp. Mech.* 53(4), 543-556.
- Morgeneyer, T., Taillandier-Thomas, T., Helfen, L., Baumbach, T., Sinclair, I., Roux, S., Hild, F., 2014. In situ 3D observation of early strain localisation during failure of thin Al alloy (2198) sheet. *Acta Mat.* 69, 78-91.
- Morgeneyer, T. F., Taillandier-Thomas, T., Buljac, A., Helfen, L., Hild, F. 2016. On strain and damage interactions during tearing: 3D in situ measurements and simulations for a ductile alloy AA2139-T3. *Journal of the Physics and Mechanics of Solids* 96, 550-571.
- Morin, L., Leblond, J.B., Tvergaard, V., 2016. Application of a model of plastic porous materials including void shape effects to the prediction of ductile failure under shear-dominated loadings. *J. Mech. Phys. Solids* 94, 148-166.
- Myagotin, A., Voropaev, A., Helfen, L., Hänschke, D., Baumbach, T., 2013. Efficient Volume Reconstruction for Parallel-Beam Computed Laminography by Filtered Backprojection on Multi-Core Clusters. *IEEE Trans. Image Process.* 22(12), 5348-5361.
- Nielsen, K. L., Dahl, J., Tvergaard, V., 2012. Collapse and coalescence of spherical voids subject to intense shearing: studied in full 3D. *International Journal of Fracture* 177 (2), 97-108.
- Pack, K., Marcadet, S.J., 2016. Numerical failure analysis of three-point bending on martensitic hat assembly using advanced plasticity and fracture model for complex loading. *Int. J. Solids and Structures* 47(9), 1130-1143.
- Papasidero J, Doquet V, Lepeer, S., 2014. Multiscale investigation of ductile fracture mechanisms and strain localization under shear loading in 2024-T351 aluminum alloy and 36NiCrMo16 steel, *Materials Science and Engineering A* 610, 203-219.
- Rice, J.R., Tracey, D.M., 1969. On the ductile enlargement of voids in triaxial stress fields. *Journal of the Mechanics and Physics of Solids* 17 (3), 201-217.
- Rice, J.R., 1976. The localization of plastic deformation, in: Koiter, W.T. (Ed.), *Theoretical and Applied Mechanics*. North Holland, Amsterdam, p.207.
- Roth, C.C., Mohr, D., 2014. Effect of strain rate on ductile fracture initiation in advanced high strength steel sheets: experiments and modeling. *Int. J. Plast.* 56, 19–44.
- Roth, C.C., Mohr, D., 2016. Ductile fracture experiments with locally proportional loading histories. *Int. J. Plast.* 79, 328-354,

- Roux, S., Hild, F., Viot, P., Bernard, D., 2008. Three dimensional image correlation from X-Ray computed tomography of solid foam. *Comp. Part A* 39(8), 1253-1265.
- Scales, M., Tardif, N., Kyriakides, S., 2016. Ductile failure of aluminum alloy tubes under combined torsion and tension. *International Journal of Solids and Structures* 97-98, 116–128.
- Scheyvaerts, F., Onck, P. R., Tekoglu, C., Pardoën, T., 2011. The growth and coalescence of ellipsoidal voids in plane strain under combined shear and tension. *J. Mech. Phys. Solids* 59, 373–397.
- Shutov, A. V., Silbermann, C.B., Ihlemann, J., 2015. Ductile damage model for metal forming simulations including refined description of void nucleation. *International Journal of Plasticity* 71, 195–217.
- Srinivasa, A. R., 2001. Large deformation plasticity and the Poynting effect. *Int. J. Plast.* 17 (9), 1189-1214.
- Steglich, D., Brocks, W., 1997. Micromechanical modelling of the behaviour of ductile materials including particles. *Comp. Mat. Sci.* 9, 7-17.
- Sutton, M.A., Orteu, J.J., Schreier, H., 2009. *Image correlation for shape, motion and deformation measurements: Basic Concepts, Theory and Applications*. Springer, New York.
- Swift, H.W., 1952. Plastic instability under plane stress. *Journal of Mechanics Physics of Solids* 1, 1–18.
- Taillandier-Thomas, T., Roux, S., Morgeneyer, T. F., Hild, F., 2014. Localized strain field measurement on laminography data with mechanical regularization. *Nuclear Instruments and Methods in Physics Research Section B* 324, 70-79.
- Tekoglu, C., Leblond, J.-B., Pardoën, T., 2012. A criterion for the onset of void coalescence under combined tension and shear. *J. Mech. Phys. Solids* 60, 1363–1381.
- Teodosiu, C., Hu, Z.Q., 1995. Evolution of the Intragranular Microstructure at Moderate and Large Strains - Modelling and Computational Significance, in: Shen, S.-F., Dawson, P. R. (Eds.), *Proceedings of the 5th International Conference on Numerical Methods in Industrial Forming Processes (NUMIFORM '95)*, Balkema, Rotterdam, pp. 173-182.
- Torki, M.E., Tekoğlu, C., Leblond, J.B., Benzerga, A.A., 2017. Theoretical and numerical analysis of void coalescence in porous ductile solids under arbitrary loadings. *International Journal of Plasticity* 91, 60-181.
- Tutyshkin, N., Müller, W. H., Wille, R., Zapara, M., 2014. Strain-induced damage of metals under large plastic deformation: Theoretical framework and experiments. *International Journal of Plasticity* 59, 133–151.
- Tvergaard, V., 1981. Influence of voids on shear band instabilities under plane strain conditions, *International Journal of Fracture* 17 (4).
- Tvergaard, V., 1990. Material failure by void growth to coalescence, *Adv. Appl. Mech.* 27., 83-151.
- Tvergaard, V., 2012. Effect of stress-state and spacing on voids in a shear-field., *Int. J. Solids Struct.* 49, 3047–3054.
- Tvergaard, V., 2015a. Behaviour of porous ductile solids at low stress triaxiality in different modes of deformation. *Int. J. Solids Struct.* 60–61, 28–34.

- Tvergaard, V., 2015b. Study of localization in a void-sheet under stress states near pure shear. *International Journal of Solids and Structures* 75–76, 134–142.
- Ueda, T., Helfen, L., Morgeneyer, T.F., 2014. In situ laminography study of three-dimensional individual void shape evolution at crack initiation and comparison with Gurson–Tvergaard–Needleman-type simulations. *Acta Mater.* 78, 254–270.
- Voce, E., 1948. The relationship between stress and strain for homogeneous deformation. *Journal of the Institute Metals* 74, 537–562.
- Vogelgesang, M., Farago, T., Morgeneyer, T. F., Helfen, L., dos Santos Rolo, T., Myagotin, A., Baumbach, T., 2016. Real-time image content based beamline control for smart 4D X-ray imaging. *Journal of Synchrotron Radiation* 23, 1254–1263.
- Wang, K., Luo, M and Wierzbicki, T., 2014. Experiments and modeling of edge fracture for an AHSS sheet, *International Journal of Fracture* 187 (2), 245–268.
- Weck, A., Wilkinson, D.S., 2008. Experimental investigation of void coalescence in metallic sheets containing laser drilled holes. *Acta Mater.* 56, 1774–1784.
- Xu, F., Helfen, L., Baumbach, T., Suhonen, H., 2012. Comparison of image quality in computed laminography and tomography. *Optics Express* 20, 794–806.
- Zhai, J., Luo, T., Gao, X., Graham, S. M., Baral, M., Korkolis, Y. P., Knudsen, E., 2016. Modeling the ductile damage process in commercially pure titanium. *International Journal of Solids and Structures* 91, 26–45.

Tables

Table 1. Material properties used for modeling FB600 (for parameter definitions, see Roth and Mohr (2014))

P_{12}	P_{22}	P_{44}	G_{12}	G_{22}	G_{44}
[-]	[-]	[-]	[-]	[-]	[-]
-0.4283	0.8564	2.7477	-0.3716	0.7848	3.1158
A	ε_0	n	k_0	Q	β
[MPa]	[-]	[-]	[MPa]	[MPa]	[-]
798.63	6.71E-03	0.096	503.67	141.24	26.81
α	E	ν	ρ		
[-]	[GPa]	[-]	[kg/m ³]		
0.646	210	0.3	7850		

Figures

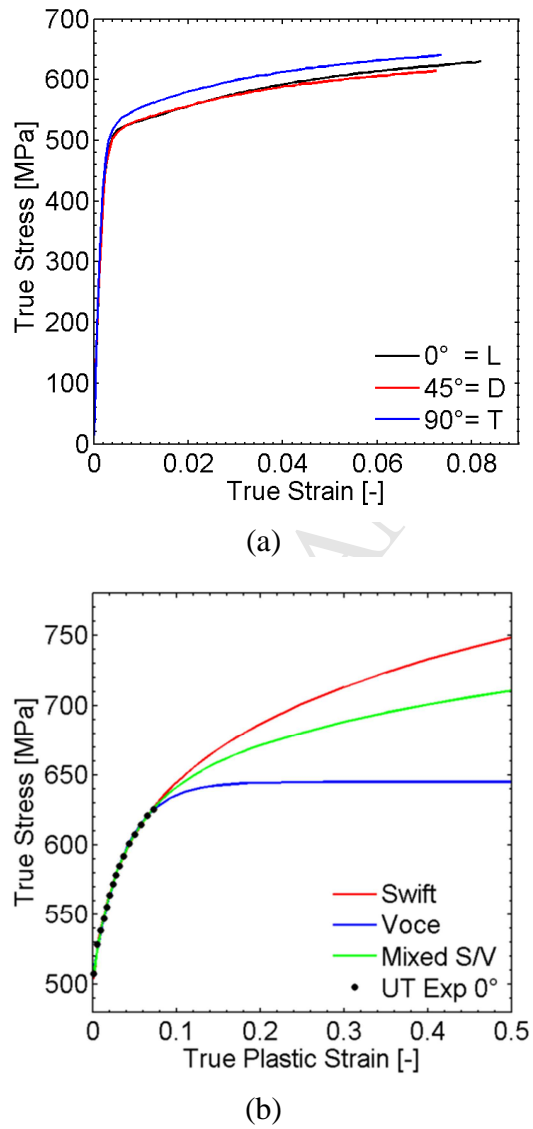


Figure 1. Plasticity of the FB600 steel: (a) True stress vs. logarithmic strain curves (from experiments) and (b) inter- and extrapolation of the hardening law (plasticity model).

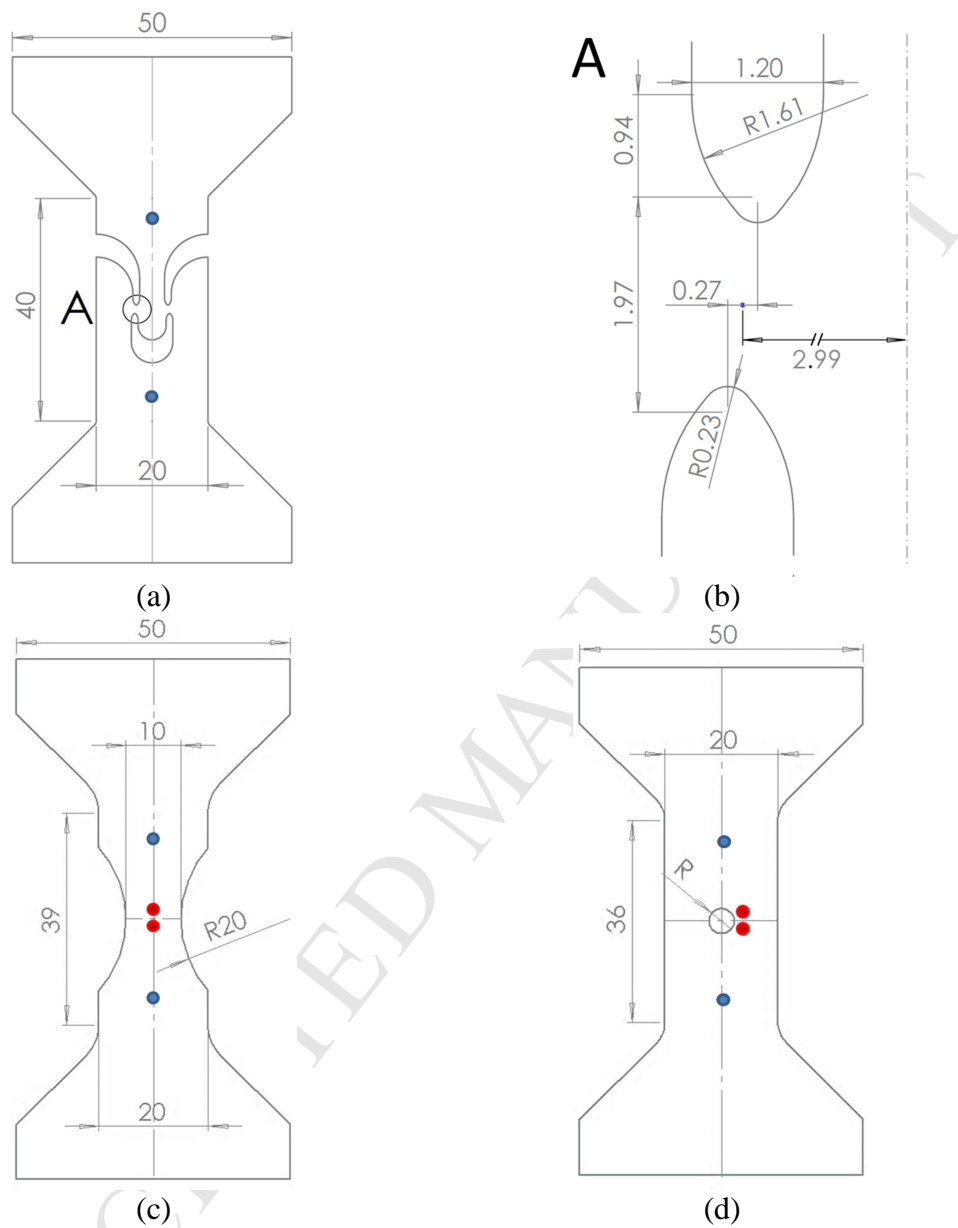
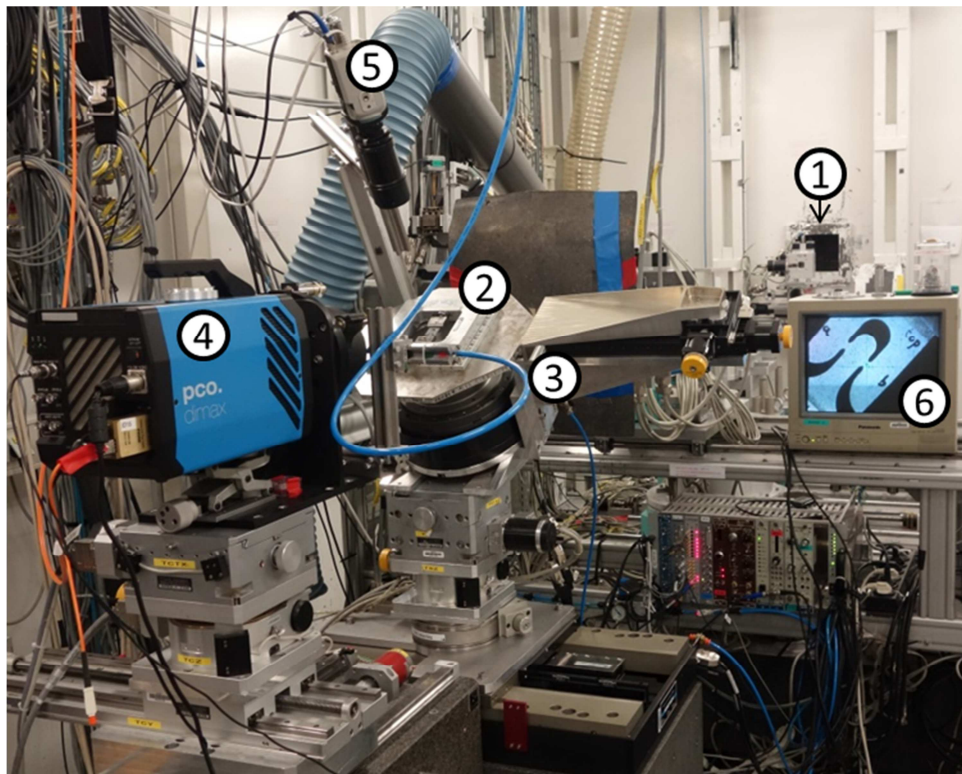
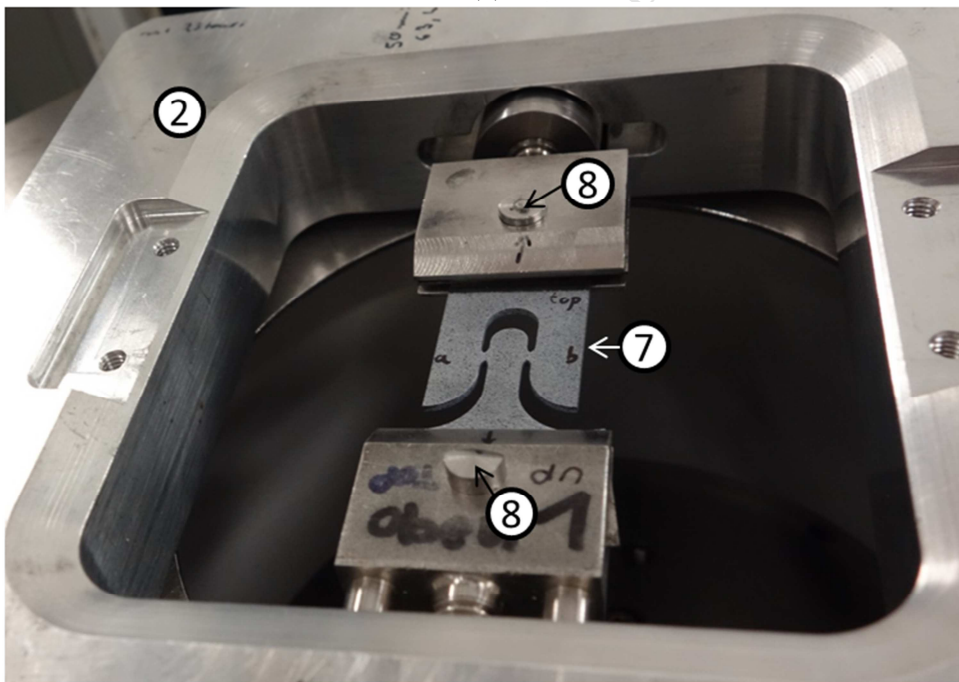


Figure 2. Fracture specimen geometries: (a) smiley shear specimen (SH), and (b) detail of the gage section geometry, (c) notched tension specimen (NT20), (d) tension specimen with a central hole of radius $R=2.5\text{mm}$ (CH). Blue solid dots highlight the position of the virtual extensometer for relative displacement measurements. Red solid dots denote the reference points for the local axial strain measurement.



(a)



(b)

Figure 3. Set-up for in-situ laminography experiments: (a) ① X-ray beam line exit, ② load frame on laminography rotation setup, ③ positioning stage, ④ camera for image acquisition, ⑤ optical camera, ⑥ image seen by optical camera and (b) close up of ⑦ SH specimen in ② load frame held by ⑧ pins.

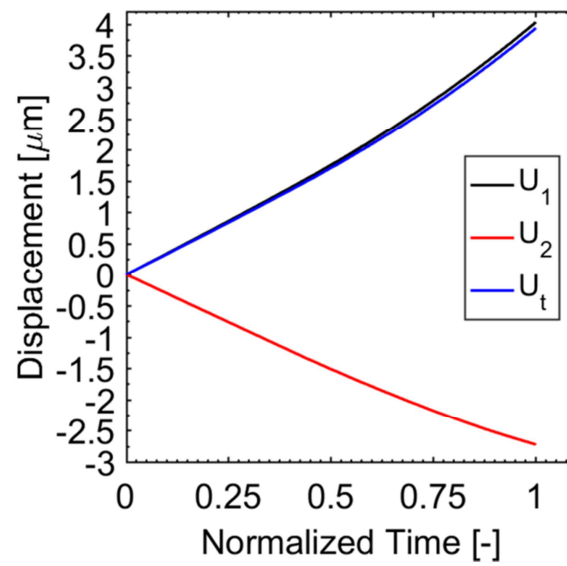
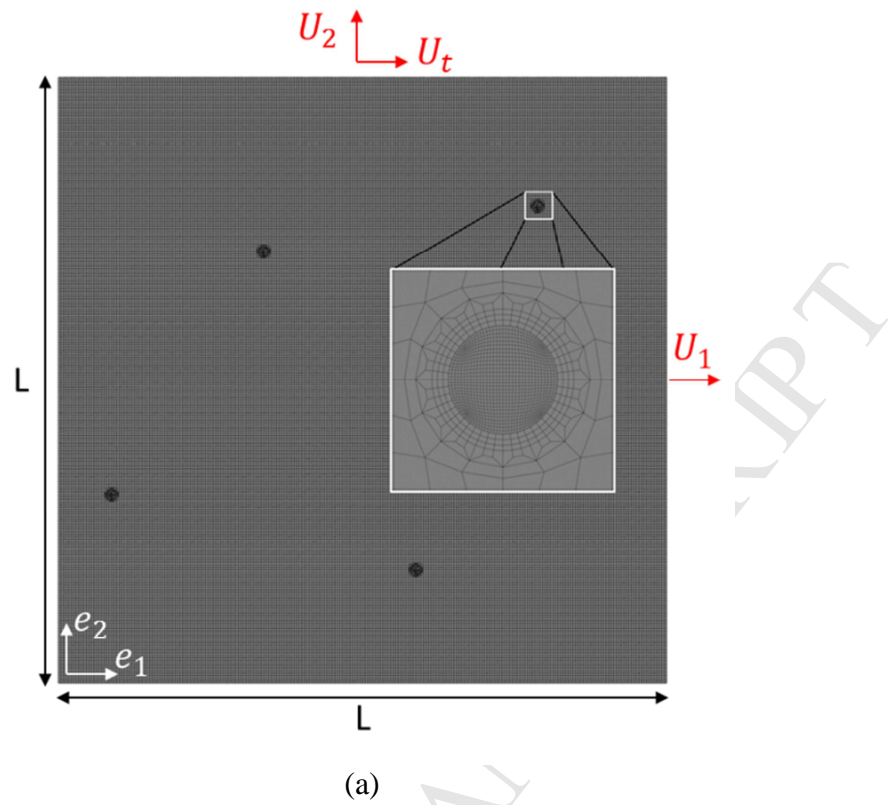


Figure 4. (a) Finite element mesh of Representative Volume Element (RVE) of the mesostructure with a particle volume fraction of 0.015%. The magnified area shows the mesh around a single particle; (b) displacement histories applied through the MPC user subroutine.

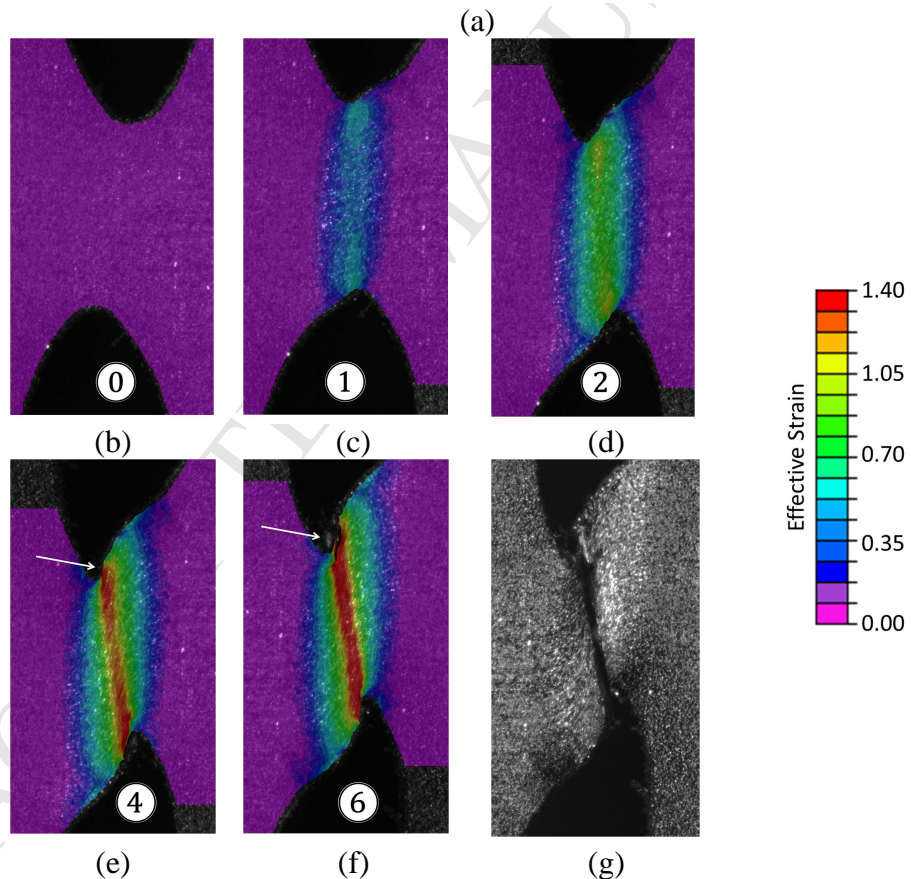
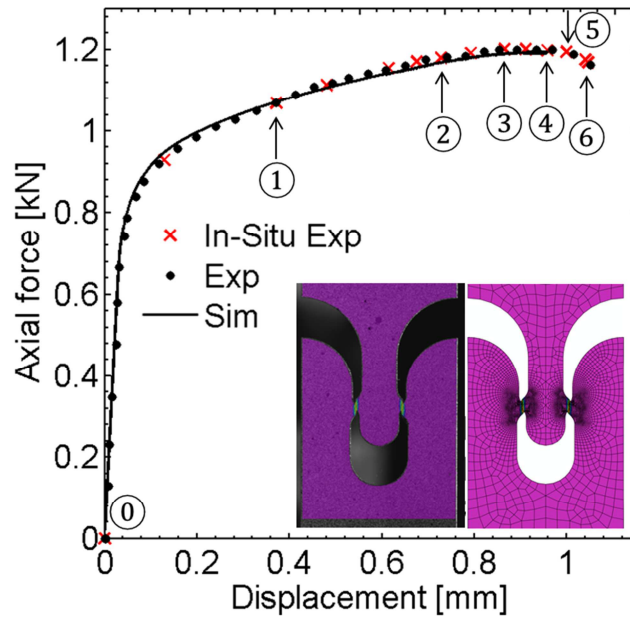


Figure 5. (a) Force-displacement curves for the macroscopic shear experiments (black dots), the in-situ shear experiments (red crosses) and the numerical simulation (solid black line). The contour plots (c)-(f) show the effective strain on the specimen surface as determined from DIC. The number labels indicate the corresponding instants in (a). (g) shows the gage section after fracture.

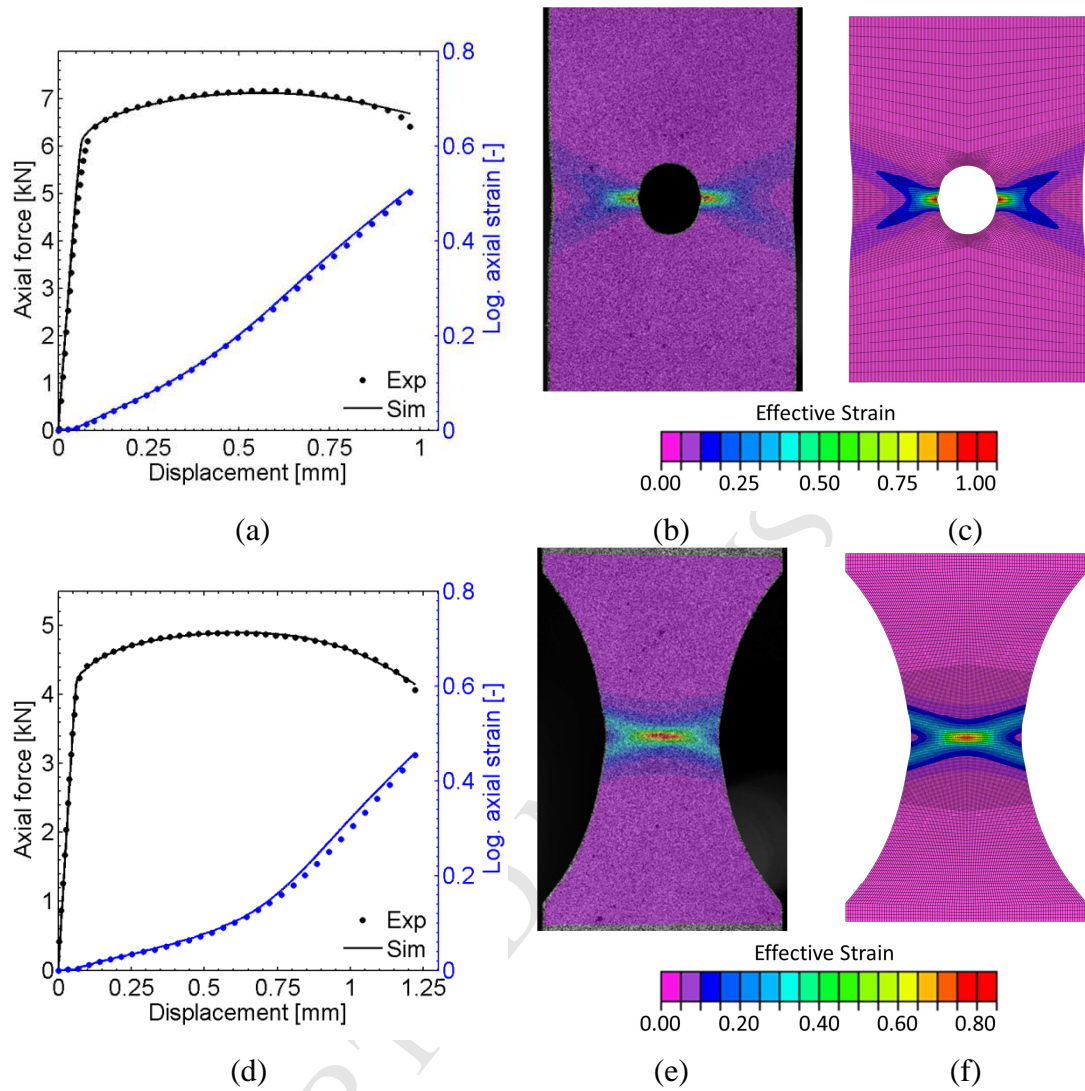


Figure 6. Results of the hybrid experimental-numerical analysis tension with a central hole $R=2.5\text{mm}$ (CH) and notched tension (NT20): (a, d) force-displacement curves (black) and local axial strain (blue); dots represent the experimental results, while solid lines denote the simulation results; effective surface strain field at the instant of fracture initiation as observed experimentally (b, e), and predicted numerically (c, f).

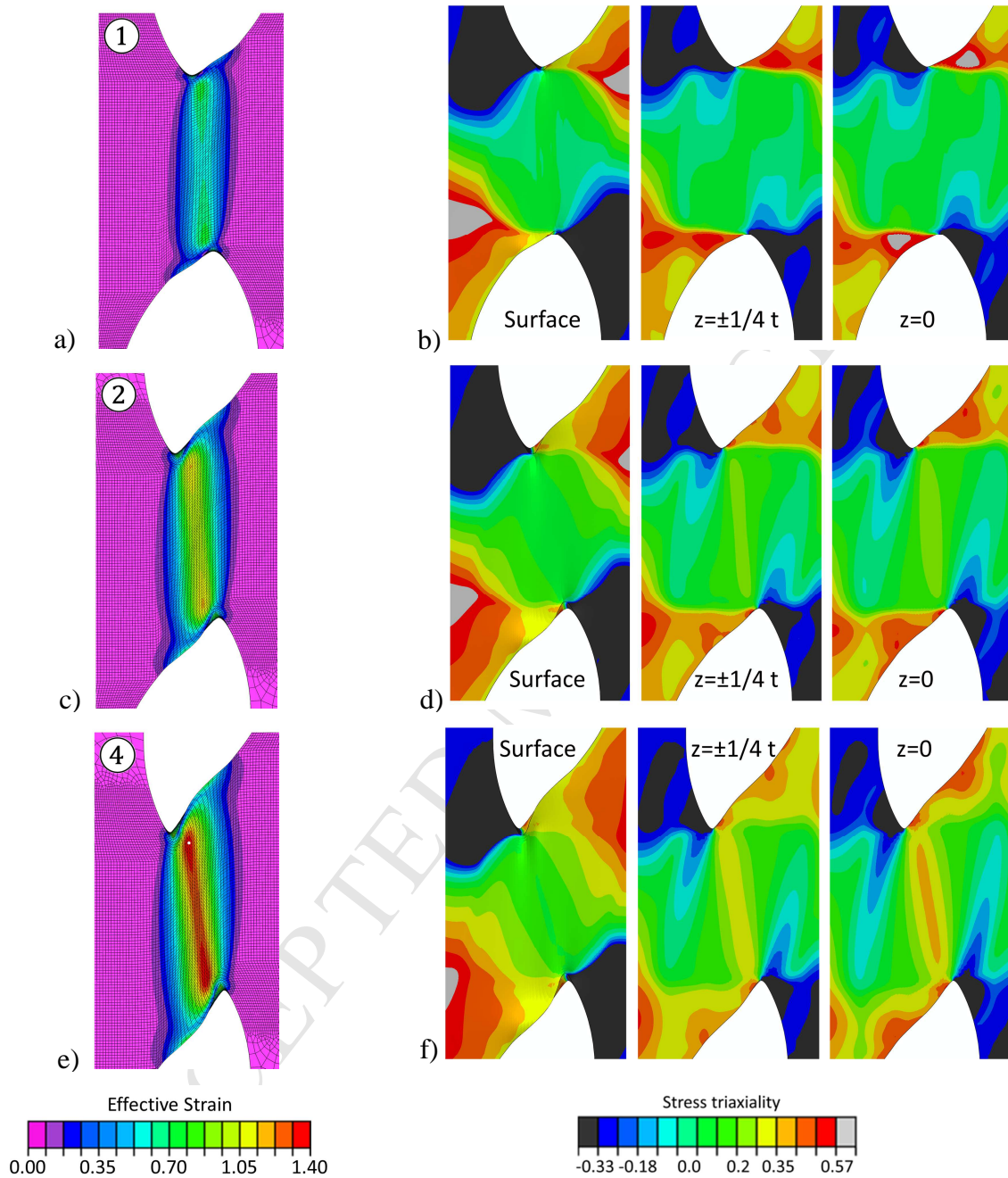


Figure 7. Simulation results for the instants ① (first row), ② (second row) and ④ (third row). The first column shows the effective strain on the specimen surface; the stress triaxiality fields are shown for the specimen surface (second column), on a plane at a distance of $1/4t$ below the surface (third column), and at the specimen mid-plane (fourth column).

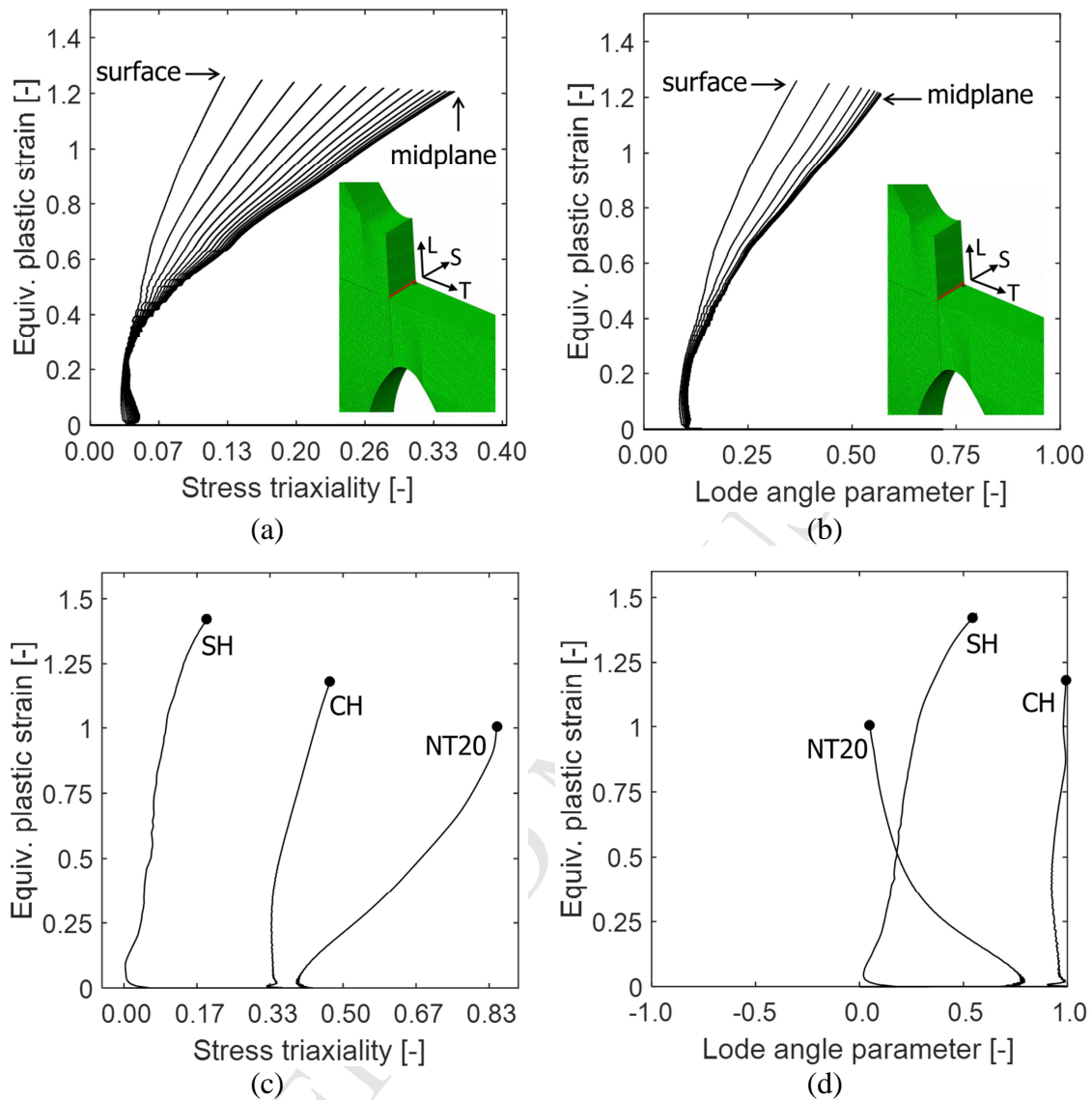


Figure 8. Loading paths as extracted from numerical simulations: results for the 16 elements in the center of the SH specimen gage section (top row), and for the element with the maximum equivalent plastic strain in the SH, CH and NT20 specimens (bottom row). The loading paths are shown in terms of the equivalent plastic strain vs. stress triaxiality (left column), and equivalent plastic strain vs. Lode angle parameter (right column).

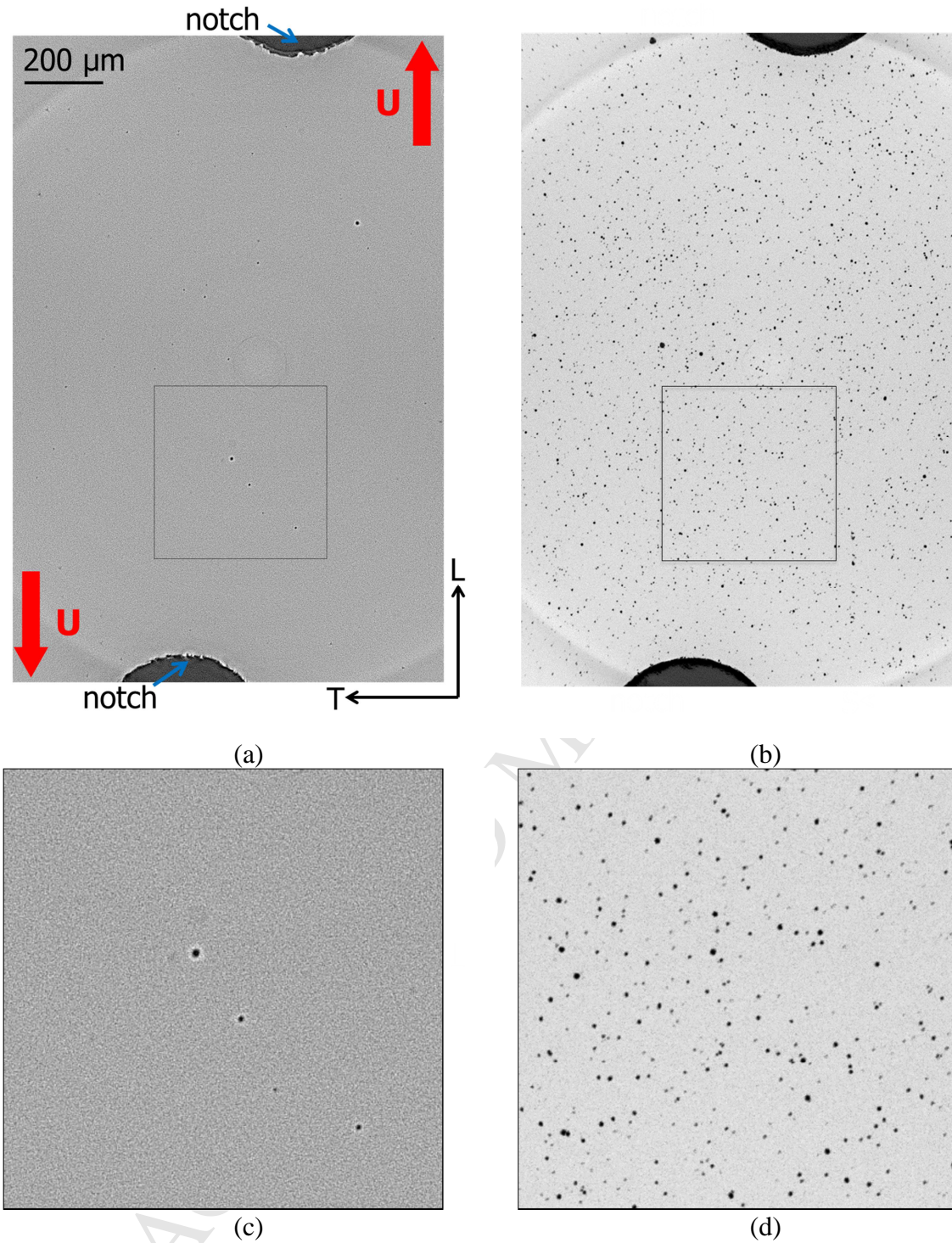


Figure 9. Laminography pictures of the initial state: (a) 2D section at mid-thickness without projection (1.095 μm thick), (b) projection of the gray value minima over a sample thickness of 438 μm . This is subsequently used for 2D digital image correlation. Enlargements of marked areas in (a) and (b) are shown in (c) and (d).

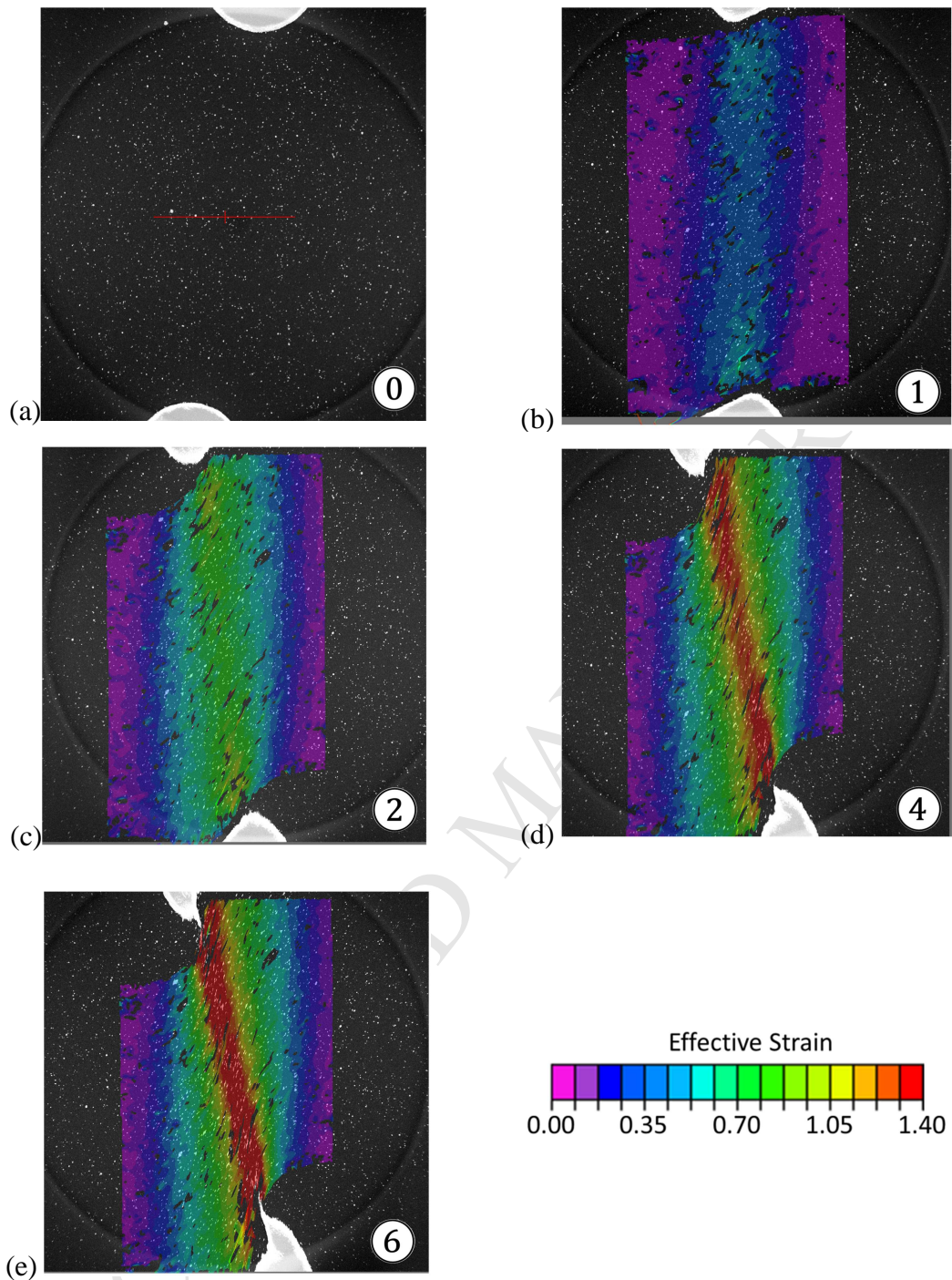


Figure 10. 2D image maximum contrast projection (inverted) resulting from a $438\ \mu\text{m}$ thick slice overlaid by the 2D digital image correlation results for cumulated effective strain for load steps as labeled in Fig 5a. The solid red line in (a) corresponds to the line segment along which the local measurement shown in Fig. 11 is taken. The gage section shown corresponds to the left gage section in Fig. 1a. The maximum strains in (e) locally attained 1.48, thereby exceeding the maximum value of the color scale bar.

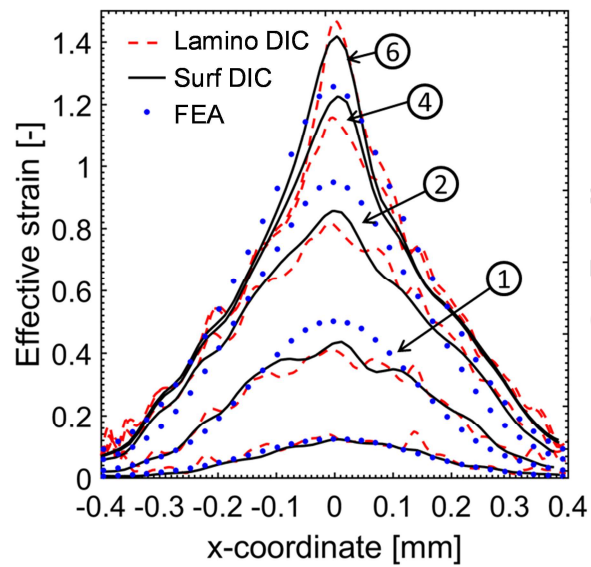


Figure 11. Comparison of the evolution of the effective strain for a line segment (red solid line in Fig 11a for the three different methods evaluated: planar surface DIC, numerical simulation and planar DIC on projected laminography images.

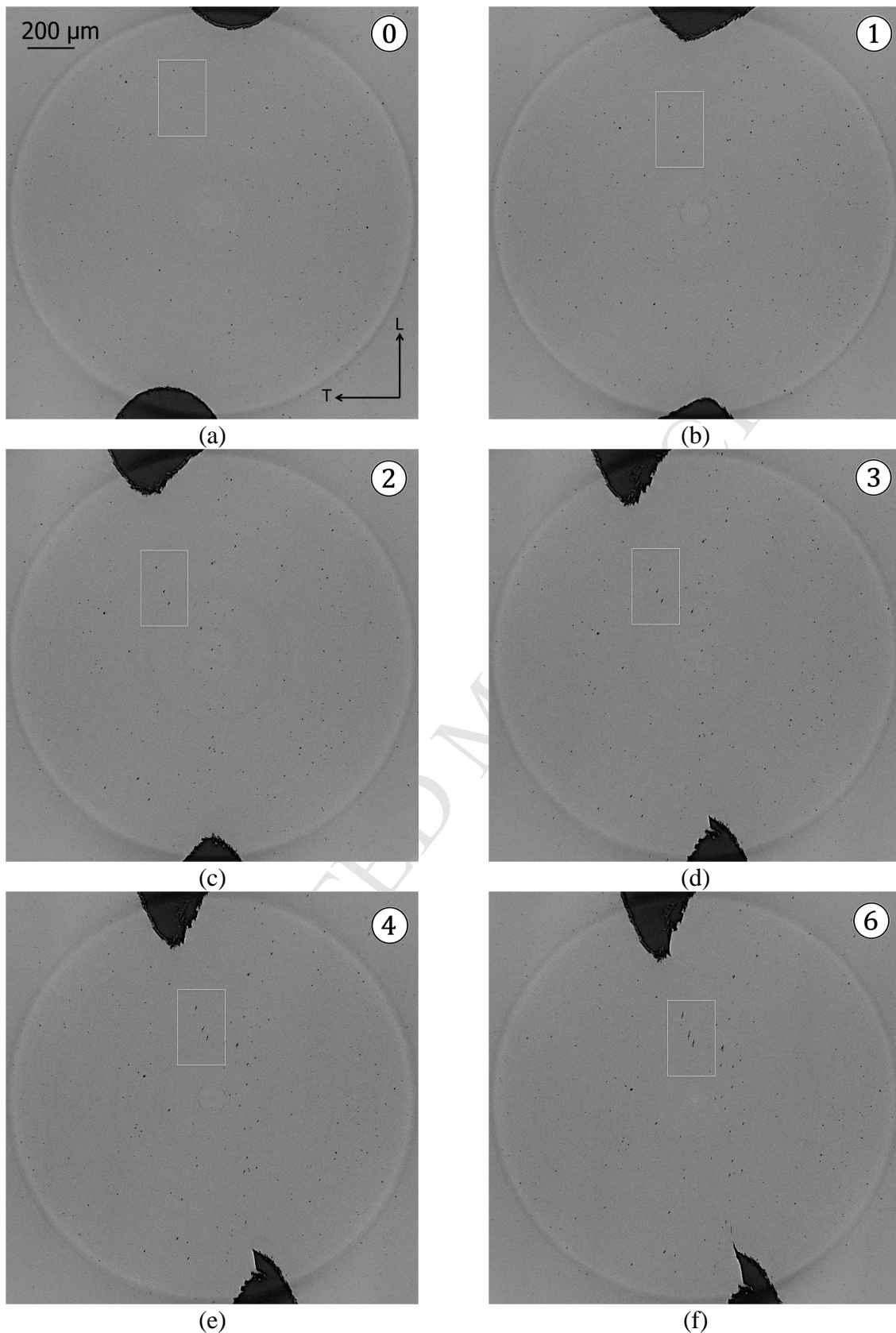


Figure 12. 2D Projection of minimum contrast in a 17 μm thick slice at specimen mid-plane for load steps as labeled in Fig 5a. Magnified images of the mesostructure inside the white rectangles are shown in Fig. 13.

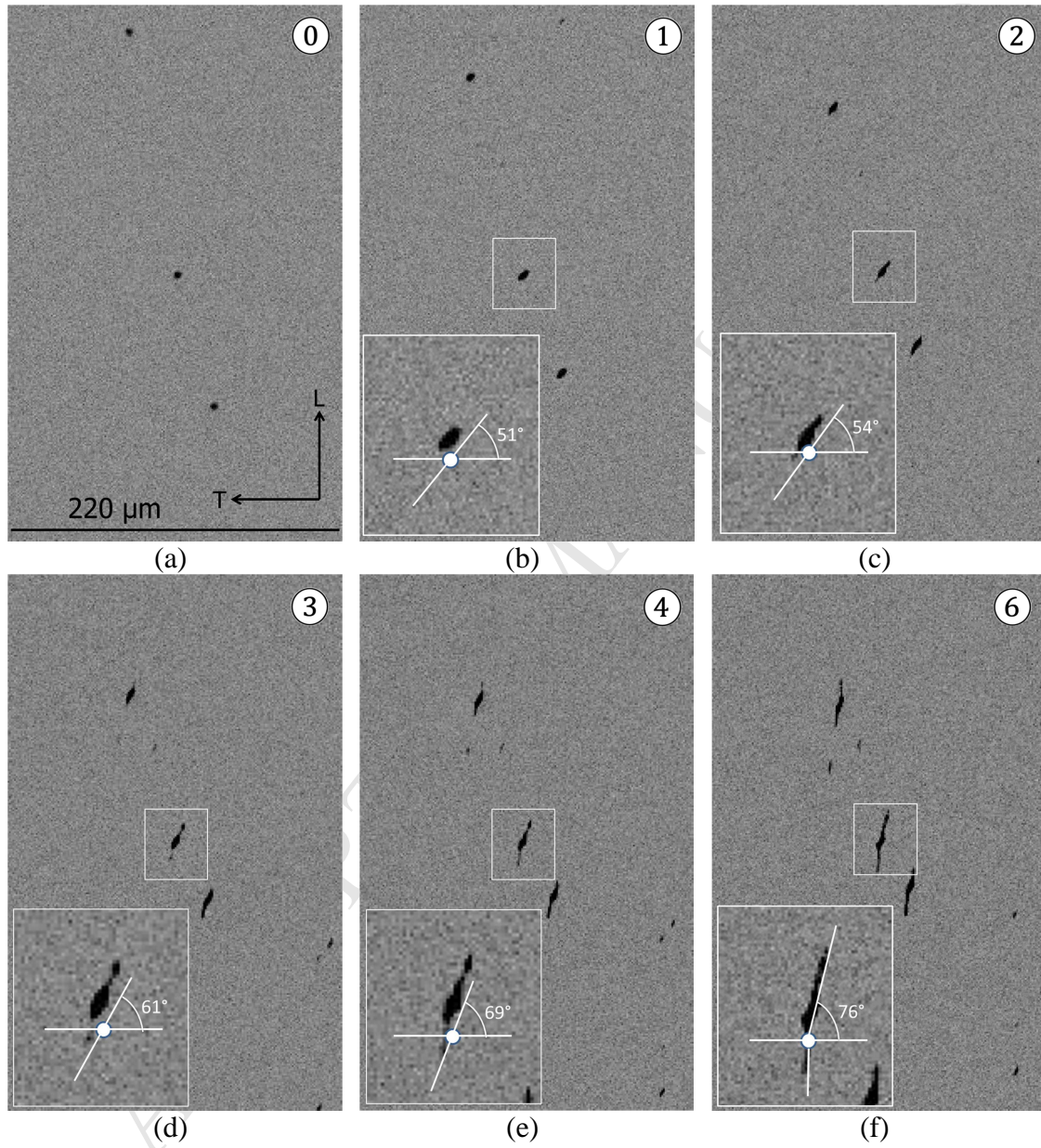


Figure 13. Magnified images of the mesostructure inside the white rectangles in the 2D projections shown in Fig. 12.

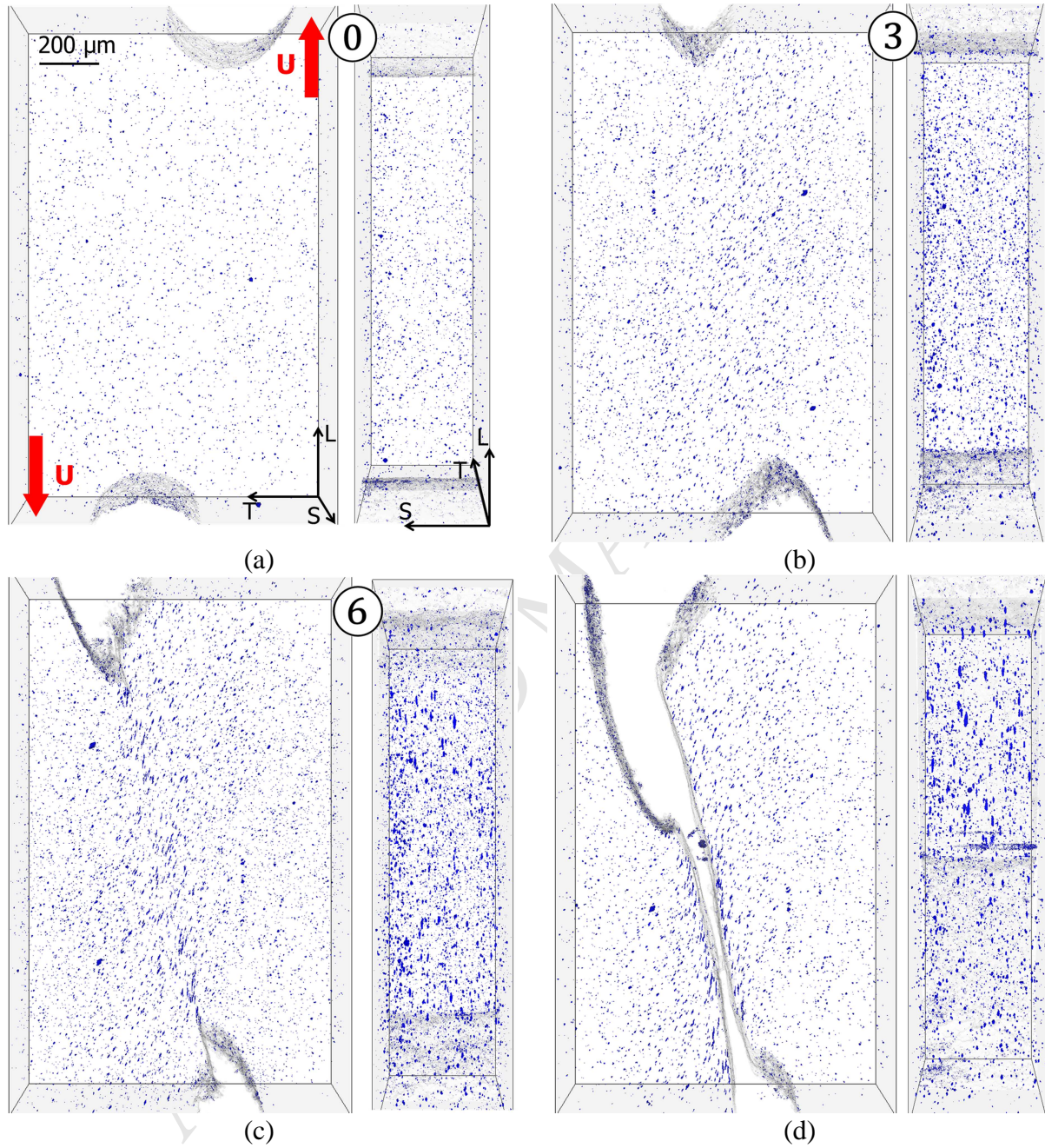
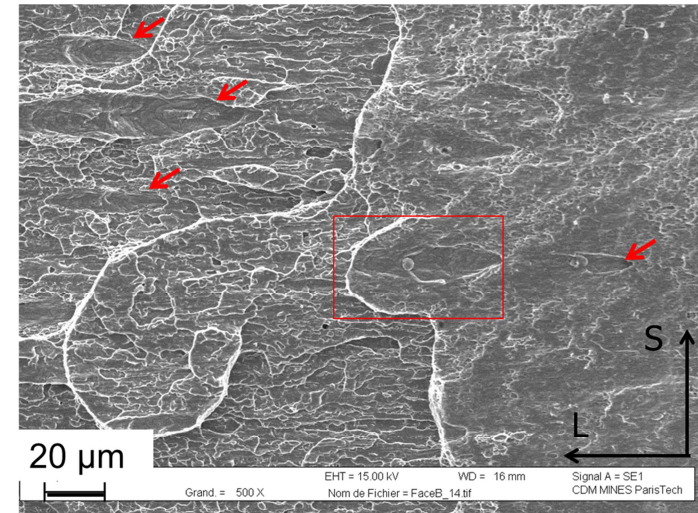
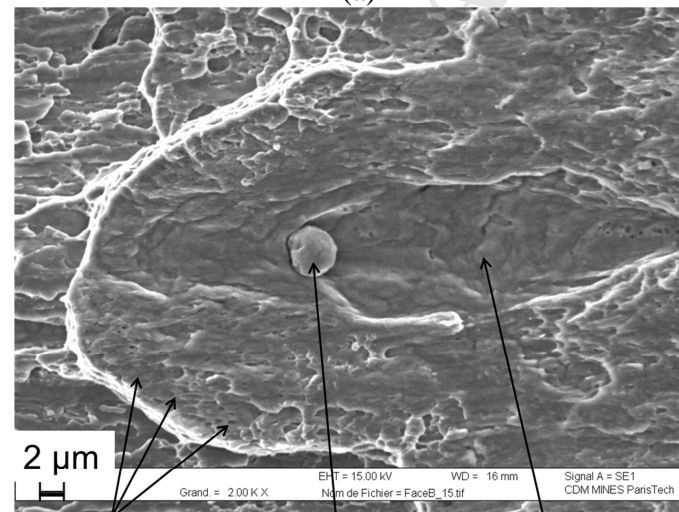


Figure 14. 3D views of a 440 μm wide and 770 μm high slice normal to the sheet at (a) instant ①, (b) instant ③, (c) instant ⑥ and (d) after final fracture. The steel matrix has been made transparent and particles and voids are colored in blue.



← Shear loading direction →

(a)



Small dimples CaO particle Large shear dimple

(b)

Figure 15. (a) SEM fractography of the shear fracture surface with several elongated, dimple-like formations. (b) A zoom on a shear void originated from a particle, as marked by the red box in (a).

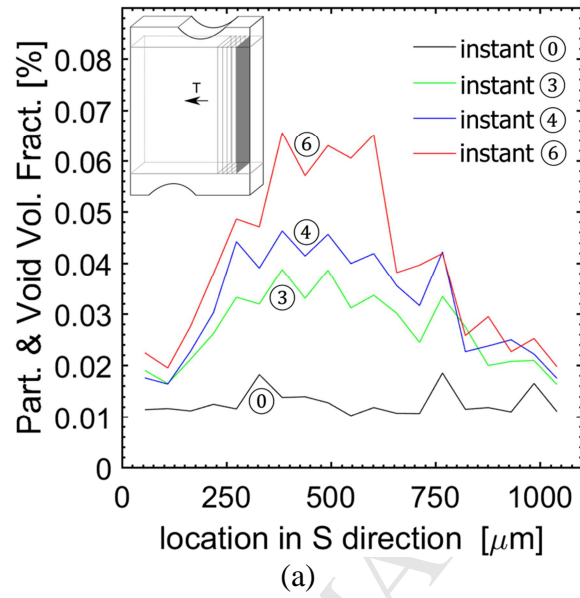


Figure 16. Sum of particle and void volume fractions in 55µm thick slices of laminography data in a 400µm deep volume along T direction for load steps as labeled in Fig 5a.

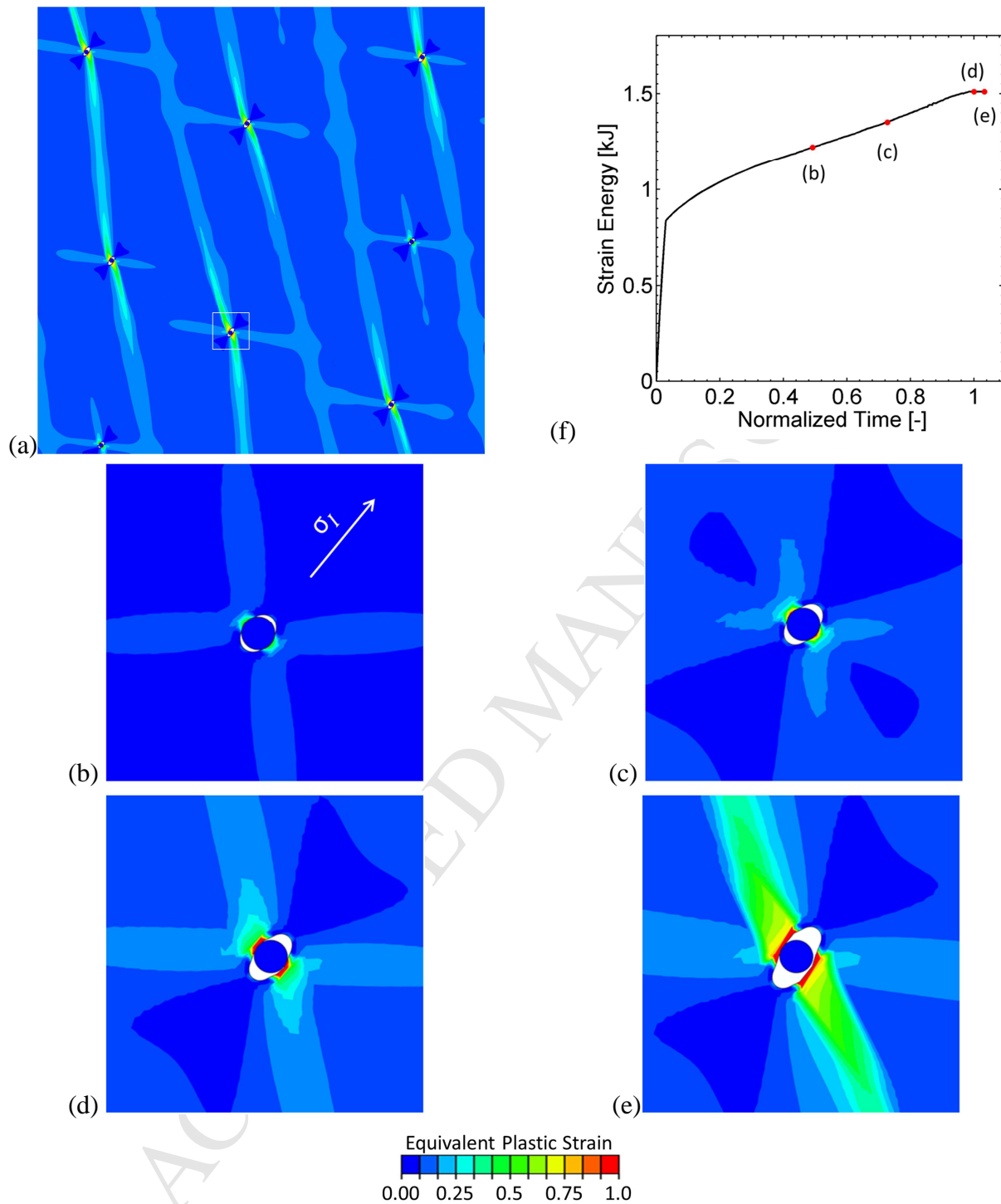


Figure 17. Results from plane stress RVE analysis with initial particle volume fraction of 0.015% for shear-dominated loading at the macroscopic level: (a) deformed mesh after onset of localization, and (b)-(e) contour plots of a particle at different states of loading, (f) total strain energy history.

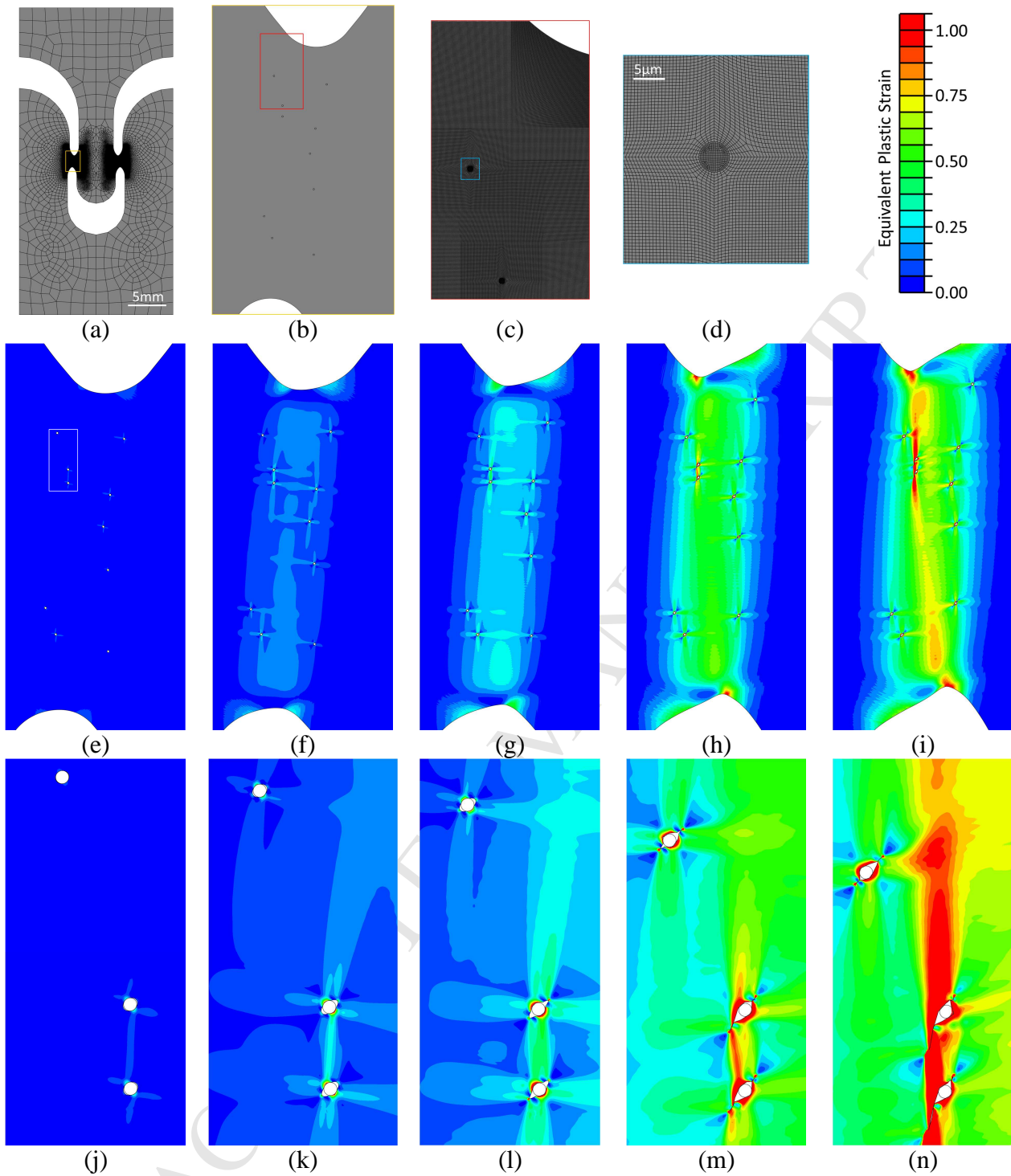


Figure 18. Results from a 2D simulation of the shear specimen with discretization of mesostructural features. (a) Finite element mesh of the whole specimen, and close ups of (b) the gage section, (c) particles close to the notch and (d) a single particle. (e)-(j) contour plots of equivalent plastic strain in the gage section, and (j)-(n) evolution of the plastic deformation around a group of particles.

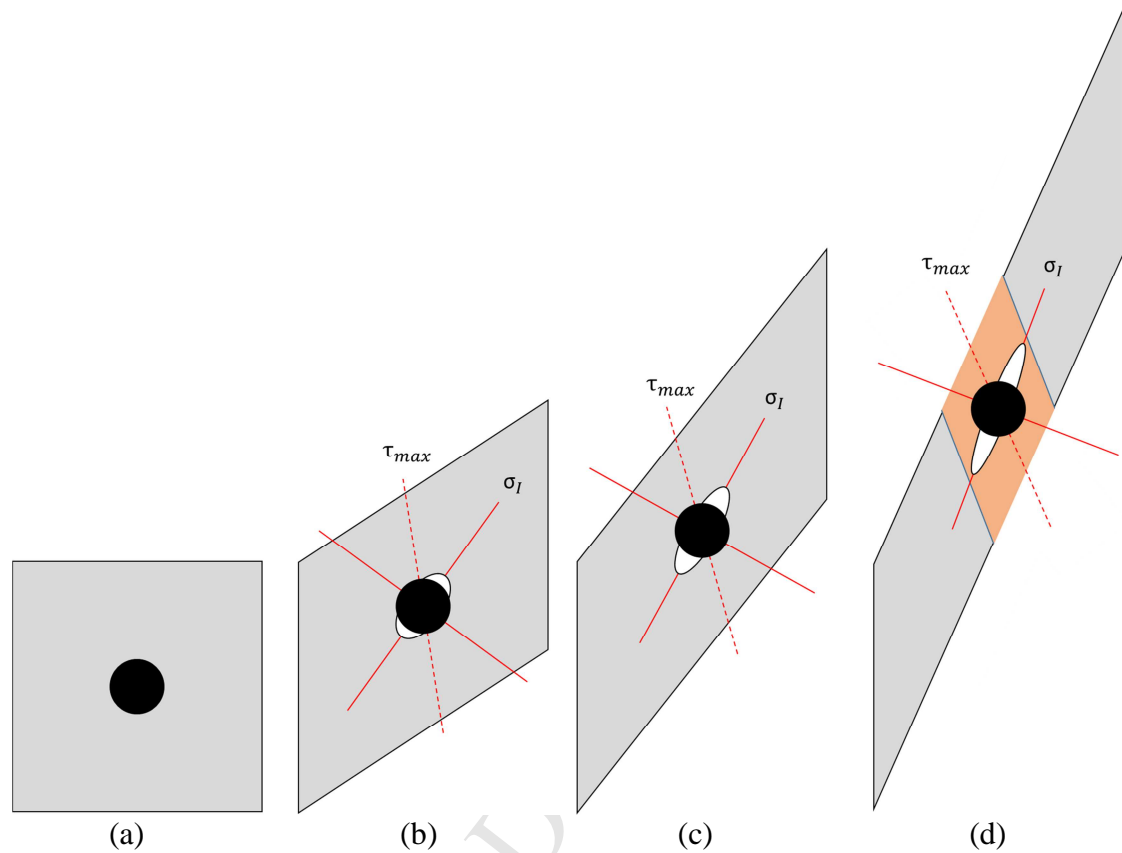


Figure 19. Schematic of simple shear failure mechanism: (a) initial state with particle in matrix material, (b) void nucleation through particle-matrix interface failure, (c) void growth along the direction of the maximum principal strain, and (d) development of a localization band close to the direction of maximum shear. The red lines highlight the directions of the principal stretches as computed from the polar and subsequent spectral decomposition of the deformation gradient.

- Determined stress-state dependent fracture initiation in a ferritic-bainitic steel with CaO particles
- Performed in-situ shear experiment on synchrotron X-ray line
- Observed void nucleation and growth under shear-dominant loading conditions
- Explained observed failure mechanism through computational shear localization analysis